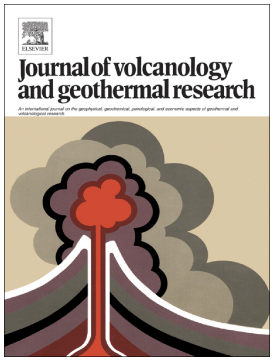

Satellite observations of fumarole activity at Aluto volcano, Ethiopia: Implications for geothermal monitoring and volcanic hazard

Mathilde Braddock, Juliet Biggs, Iain M. Watson, William Hutchison, David M. Pyle, Tamsin A. Mather

PII: S0377-0273(17)30118-X
DOI: doi: 10.1016/j.jvolgeores.2017.05.006
Reference: VOLGEO 6091

To appear in: *Journal of Volcanology and Geothermal Research*

Received date: 24 February 2017
Revised date: 6 May 2017
Accepted date: 7 May 2017

Please cite this article as: Mathilde Braddock, Juliet Biggs, Iain M. Watson, William Hutchison, David M. Pyle, Tamsin A. Mather , Satellite observations of fumarole activity at Aluto volcano, Ethiopia: Implications for geothermal monitoring and volcanic hazard, *Journal of Volcanology and Geothermal Research* (2017), doi: 10.1016/j.jvolgeores.2017.05.006

Satellite observations of fumarole activity at Aluto volcano, Ethiopia: implications for geothermal monitoring and volcanic hazard

Mathilde Braddock[1]*, Juliet Biggs[2], Iain M. Watson[2], William Hutchison[3], David M. Pyle[4] and Tamsin A. Mather[4]

[1] School of Earth Sciences, University of Bristol, Wills Memorial Building, Queens Road, Bristol BS8 1RJ, UK
[2] COMET, School of Earth Sciences, University of Bristol, Wills Memorial Building, Queens Road, Bristol BS8 1RJ, UK
[3] School of Earth and Environmental Sciences, University of St. Andrews, KY16 9AL, UK
[4] COMET, Department of Earth Sciences, University of Oxford, Oxford, UK

*Corresponding author: mb12815@my.bristol.ac.uk

Abstract

Fumaroles are the surface manifestation of hydrothermal circulation and can be influenced by magmatic, hydrothermal, hydrological and tectonic processes. This study investigates the temporal changes in fumarole temperatures and spatial extent on Aluto, a restless volcano in the Main Ethiopian Rift (MER), in order to better understand the controls on fluid circulation and the interaction between the magmatic and hydrothermal systems. Thermal infrared (TIR) satellite images, acquired by the Advanced Spaceborne Thermal Emission and Reflection radiometer (ASTER) over the period of 2004 to 2016, are used to generate time series of the fumarole temperatures and areas. The thermal anomalies identified in the ASTER images coincide with known fumaroles with temperatures > 80°C and are located on or close to fault structures, which provide a pathway for the rising fluids. Most of the fumaroles, including those along the major zone of hydrothermal upwelling, the Artu Jawe Fault Zone, have pixel-integrated temperature variations of only ~2 ± 1.5°C. The exception are the Bobesa fumaroles located on a hypothesised caldera ring fault which show pixel-integrated temperature changes of up to 9°C consistent with a delayed response of the hydrothermal system to precipitation. We conclude that fumaroles along major faults are strongly coupled to the magmatic-hydrothermal system and are relatively stable with time, whereas those along shallower structures close to the rift flank are more strongly influenced by seasonal variations in groundwater flow. The use of remote sensing data to monitor the thermal activity of Aluto provides an important contribution towards understanding the behaviour of this actively deforming volcano. This method could be used at other volcanoes around the world for monitoring and geothermal exploration.

Keywords: temperature, fumaroles, Aluto, Main Ethiopian Rift, ASTER

1. Introduction

Volcanoes show signs of unrest in a variety of ways, such as deformation, seismicity or hydrothermal activity. In many cases, unrest does not precede an eruption and it is essential to distinguish baseline levels of activity from the signals that might be precursory to an eruption (e.g. Fournier et al., 2010; Parks et al., 2015; Biggs et al., 2016; Coco et al., 2016). The interaction between magmatic and hydrothermal systems creates complex signals, particularly in terms of the deformation, which make it difficult to interpret the cause of the unrest (e.g. Gottsmann et al., 2006; Lowenstern & Hurwitz, 2008; Coco et al., 2016; Hemmings et al., 2016). Fumaroles offer an important window into the processes at work beneath the surface of a volcano and some studies have suggested that monitoring changes in the composition and temperature of the gases they emit might aid in the prediction of changes in volcanic activity (Madonia & Fiordilino, 2013; Laiolo et al., 2017). The fluids released at the fumaroles have undergone a long journey: escaping from the magma, travelling up through the rocks and the shallow hydrothermal and groundwater systems to reach the surface. As a result, the fumarolic fluids provide information that with careful interpretation can yield to insights into the interaction between the magmatic and hydrothermal systems (Fournier, 1999; Ingebritsen et al., 2010; Laiolo et al., 2017).

Fluid flow in hydrothermal systems is controlled by many overlapping processes, which are unique to each system: the thermal gradient, the anisotropy of the permeability (Arnórsson, 1995), the precipitation of secondary minerals (Lowell et al. 1993), the availability of groundwater for recharge, the local topography (Hurwitz et al. 2003), and the phases present in the system (Ingebritsen & Sorey, 1988). In some cases, both precipitation and groundwater flow are known to have an influence on the temperature of fumaroles (Richter et al. 2004), but not in others (Connor et al., 1993; Di Liberto, 2011). These examples demonstrate the highly individual behaviour of the hydrothermal systems at volcanoes and emphasize the necessity for a careful understanding of the subsurface structures and the parameters that control groundwater flow in each individual scenario.

Aluto, a typical caldera volcano of the Main Ethiopian Rift (MER), is currently showing signs of unrest, including seismicity (Wilks et al., 2017) and ground deformation (Biggs et al., 2011; Hutchison et al., 2016a). In this study, we use satellite remote sensing to analyse the changes in behaviour of the fumaroles on Aluto in an attempt to further understand the causes of the unrest. When considering how interactions between the magmatic and hydrothermal systems might be observed at the surface from changes in the behaviour of the fumaroles, two end-member scenarios may be proposed, depending on whether changes in the hydrothermal system are driven by hydrological factors ("top-down") or magmatic processes ("bottom-up"):

1) "top-down" scenario: the fumaroles are only connected to the shallow hydrothermal system and the changes they display are linked solely to hydrological processes such as precipitation and

groundwater flow. The hydrothermal system is heated by the deeper magmatic system, but the changes in the magmatic system are not reflected in the behaviour of the fumaroles. From observations at other volcanoes, the temperatures are expected to decrease during the rainy season due to the addition of cold rain water to the groundwater flow (Richter et al. 2004; Di Liberto, 2011);

2) "bottom-up" scenario: the magmatic and hydrothermal systems are linked and an increase in fumarole temperature is expected in periods of increased magmatic activity (unrest episodes), whereas a decrease will accompany a deflating trend caused by a cooling and crystallisation of the underlying magma body (Chiodini et al., 2011; D'Auria et al., 2011).

Satellite remote sensing is ideal for looking at hazardous and remote areas of the planet such as volcanoes (Pyle et al., 2013). The Advanced Spaceborne Thermal Emission and Reflection radiometer (ASTER) onboard NASA's Terra satellite has been used to investigate eruptive and thermal activity at volcanoes around the world (Pieri & Abrams, 2004), such as in South America (Jay et al. 2013) and in the Northern Pacific (Dehn et al., 2000, 2002; Pieri & Abrams, 2005; Carter & Ramsey, 2009). The detection of thermal anomalies at volcanoes is strongly dependent on the intensity and size of the anomaly, as well as its duration relative to the frequency of observation (Pieri & Abrams, 2005). Although the detection of low-temperature fumaroles (<100°C) can be done (e.g. Jay et al., 2013), the lower limit of detection of the ASTER instrument has yet to be determined (Pieri et al., 2005).

In this study, ASTER thermal infrared (TIR) images are used: 1) to detect the low-temperature fumarole activity on an active volcano and quantify the spatio-temporal limits of our current sensors in relation to monitoring and geothermal exploration; 2) to observe changes in temperature and spatial extent of the fumaroles on Aluto, understand how these relate to the other signs of unrest and evaluate the interaction between the hydrothermal and magmatic systems; 3) to quantify the subpixel temperature and spatial variations necessary to cause the changes in pixel-integrated temperatures observed.

2. Background

2.1. Regional setting

The Main Ethiopian Rift (MER)extends over 500 kilometres and forms the northernmost segment of the East African Rift system, from the Afar depression in the North to the Turkana basin in the South (Corti, 2009) (***Figure 1***). Two major sets of faults are present in the MER: (i) the boundary faults, which are long and characterised by large vertical offsets, and (ii) smaller internal faults that cut obliquely through the centre of the rift valley; these fault systems are well expressed in the northern MER (NMER), where they are characterised by a NE-SW and NNE-SSW directions, respectively. (Corti, 2009; Agostini et al., 2011a, **Figure 1**). The latter are collectively called the Wonji Fault Belt

(WFB) and accommodate the majority of the current tectonic extension in the MER (Chorowicz, 2005; Agostini et al., 2011b). The MER is tectonically active, extending in an E-W direction at a rate of 4-6 mm/yr (Stamps et al., 2008; Kogan et al. 2012; Saria et al., 2014).

The MER is lined by silicic volcanoes (***Figure 1)*** and although several of these are showing InSAR evidence for unrest (Biggs et al., 2011; Hutchison et al., 2016a), very little is known about their recent eruptive histories (Aspinall et al., 2011; Hutchison, 2016b; Vye-Brown et al., 2016; Wadge et al., 2016). Although unrest has been observed at several MER volcanoes, no confirmed historical eruptions have occurred since 1810-30, which took place at Fantale and Kone volcanoes (Gibson, 1974; Gouin, 1979; Rampey et al., 2010; Biggs et al., 2011; Wadge et al., 2016).

2.2. Aluto volcano

Aluto is silicic peralkaline volcano located in the Central Main Ethiopian Rift (CMER) (***Figure 1***).Aluto has been in a phase of post-caldera volcanism since 55 ±19 ka (Hutchison et al., 2016b) and its youngest volcanic deposits are a series of obsidian coulees and pumice domes, the most recent of which were likely erupted ~400 years ago (Hutchison et al., 2016b, 2016c). Aluto has been showing many signs of unrest in the form of surface hydrothermal activity, episodic ground deformation (Biggs et al., 2011; Hutchison et al., 2016a) and seismic activity (Wilks et al., 2017).

Interferometric Synthetic Aperture Radar (InSAR) studies have shown that over the last 12 years, Aluto has undergone two phases of rapid uplift in 2004 and 2008 interspersed with episodes of slow subsidence (Biggs et al., 2011) (***Figure 2***) and since 2009, Aluto has been slowly subsiding (Hutchison et al., 2016a). The deformation pattern has an elliptical shape centred on the volcano, extending beyond the inferred caldera ring faults. The source has been modelled as a point source located at 5.1 ± 0.3 km depth (Hutchison et al., 2016a), supported by a recent geochemical study (Gleeson et al., 2017). However, the deformation data alone do not enable the density and/or composition of the intruding fluids (i.e. magmatic, aqueous or gaseous) to be determined (Hutchison et al., 2016a).

2.3. The hydrothermal system at Aluto

Most of the information relating to Aluto's hydrothermal system originates from geothermal exploration undertaken since the 1980s during which data on the deep stratigraphy and the hydrothermal system were collected (Kebede et al., 1985; ELC Electroconsult, 1986; Teklemariam et al., 2000). During the initial exploration phase, eight deep geothermal wells were logged to produce a

cross-section of the stratigraphy (Kebede et al., 1985; ELC Electroconsult, 1986; Gizaw, 1993; Gianelli and Telkemariam, 1993). The boreholes suggested that the geothermal reservoir is located >2km beneath the surface, within the Neogene ignimbrites (geological unit Nqui, Hutchison et al., 2016b) and the fractured Bofa basalts (geological unit Nqub, Hutchison et al., 2016b) (Gizaw, 1993; Gianelli and Telkemariam, 1993; Saibi et al., 2012; Hutchison et al., 2016a). The hottest fluids were found at the bottom of well LA-3 (**Figure 3a**), with temperatures reaching 360˚C (Gebregzabher, 1986; Gizaw, 1993), and this site was chosen for the Aluto geothermal project (Hochstein et al., 2017). A pilot geothermal power plant was built in 1999 and is currently undergoing expansion to increase total power production to 70 MW (Kebede, 2014).

Previous studies have shown that the ground temperatures of the fumaroles are between 65°C and 95°C (Kebede et al., 1985; Hutchison et al., 2015, 2016c) (***Table 1***). Many of the fumaroles are located on faults suggesting that fluid flow in the shallow hydrothermal system is structurally controlled (Gizaw 1993; Gianelli and Telkemariam, 1993). CO_2 gas flux measurements constrain the upflow zone to the area beneath the Artu Jawe Fault Zone (AJFZ), a NNE-SSW trending normal fault that cuts through the Aluto caldera and belongs to the regional WFB (Hutchinson et al., 2015, 2016a). The $\delta^{18}O$ analysis of the geothermal fluids from the Aluto-Langano area reveals that >90% of the water originates from rainfall on the rift flanks and <10% comes from the lakes surrounding Aluto (Darling et al., 1996). These values highlight the importance of the precipitation on Aluto's hydrothermal system.

3. Data and methods

The ASTER instrument measures the radiance of the Earth's surface in three visible and near infrared channels (VNIR=0.5-0.8 microns), six short-wave infrared channels (SWIR=1.6-2.4 microns) and five thermal infrared channels (TIR=8-12 microns) (Pieri & Abrams, 2004). ASTER acquires images that span an area of 60×60 km and the spatial resolution of the images is 15 m per pixel in the VNIR, 30 m in the SWIR and 90 m in the TIR (Pieri & Abrams, 2004).

ASTER is well suited for observing co- or post-eruptive thermal anomalies at volcanoes, such as eruption plumes or lava flows, due to its appropriate spatial and temporal resolutions (revisit time of five days at the Equator) (Pieri & Abrams, 2004; 2005). ASTER images can also be used to detect lower amplitude thermal anomalies, such as fumaroles (Pieri & Abrams, 2005; Jay et al., 2013; Vaughan et al., 2014). The fumaroles at Aluto fall into the category of low-amplitude thermal features, as the temperatures measured on the ground range between 65°C and 95°C (Kebede et al., 1985; Hutchison et al., 2015).

3.1. Primary dataset

The ASTER data products used for this study are the level 1B (ASTL1B) images, which contain radiometrically calibrated and geometrically co-registered image data; the AST05 surface emissivity and the AST08 surface kinetic temperature products. The AST05 and AST08 products are extracted using the Temperature/Emissivity Separation algorithm (TES), which estimates the emissivity from the atmospherically corrected TIR data using the Normalized Emissivity Method (Gillespie et al., 1999). The surface kinetic temperature can be calculated from the emissivity using Planck's law and has an accuracy of ±1.5 K (Gillespie et al., 1999). Only the night-time TIR images are used in this study, as anomalously hot areas are easier to identify when the solar ground heating effect is removed. Due to ASTER's low duty cycle (8% average data collection time per orbit) (Salomonson et al., 2010), the temporal distribution of the images is very variable. The ASTER Volcano Archive website lists 63 night-time TIR images from 28/06/2000 to 07/02/2016. Out of the 63 night-time images taken over the 16 year period, only 13 were selected for processing (21 % of useable images); the rest were unusable due to cloud cover or because they only partially imaged the volcano.

The georeferencing of the ASTER night-time TIR images is known to be offset on the order of 0 to 1 pixel in latitude and 0 to 9 pixels in longitude (Vaughan et al., 2014). In order to correct for this, the images were imported into ESRI ArcGIS and orthorectified manually using ground control points (GCP) from a georeferenced Google Earth image of the area, the USGS Shuttle Radar Topographic Mission 30 m resolution digital elevation model (SRTM 30m DEM) and a 2 m resolution lidar image of Aluto (Hutchison et al., 2015, 2016b). Due to the relatively low spatial resolution of the TIR images (90 m pixel^{-1}), it was not always possible to identify identical features in all the images so the images were orthorectified using several sets of GCP resulting in a slight offset between the images of the order of ±1 pixel. The average root mean square (RMS) residual error based on the GCP orthorectification is in the range 19.51– 69.13 m, which is below the 90 m pixel resolution of the images.

3.2. Identification of the fumaroles

The ASTER TIR images are sensitive to several parameters and therefore detect other hot features as well as fumaroles. Relatively recent obsidian lava flows lack vegetation cover (Hutchison et al., 2015) and this means that they absorb and re-emit infra-red radiation strongly so appear hot in the images (Saemundsson, 2010) (***Figure 3b***). Topography and altitude also affect the temperature with elevated areas being colder and the plains being generally warmer. For these reasons, it is essential to subtract the local background temperature from each fumarole area in order to extract the temperature above background (or ΔT) of the fumarole. The background temperatures for each fumarole area were

obtained by calculating the mean of a 5×5 pixel area, chosen as close as possible to the fumaroles without resampling any of the pixels included in the fumarole areas themselves, following Vaughan et al. (2014). Google Earth images were used to identify areas within the same altitude range and with a similar vegetation cover in order to preserve the same background conditions as the fumaroles.

Our criteria for the identification of the fumaroles were clusters of >3 pixels >2°C above background temperature, seen in more than 2 images. Each potential fumarole area detected was compared to the geological map of the area to rule out other origins for the hot pixels, such as the topography or the background geology (Saemundsson, 2010; Vaughan et al., 2014). The areas located in the images were also compared to the location of fumaroles and hot springs identified on the ground (Kebede et al., 1985) (**Table 1**).

3.3. Quantification of the temperature and spatial changes at the fumaroles

Once the relevant fumarole areas were identified, a bounding area was traced around the fumaroles, 4×4 or 5×5 pixels in size, and the temperature data within these boxes was extracted for each image. The areas were chosen to cover a much larger area than the fumaroles themselves, in order to reduce the subjectivity in the choice of location of the fumaroles and to account for the offset in the orthorectification of the images.

To look at the change in temperature of the fumaroles over time, the value of the hottest pixel from each fumarole area was extracted for each image, thought to represent the temperature of the hottest and most active part of the fumarole. The background temperature specific to each fumarole area was subtracted from the hottest pixel value. These values were used to plot the time series of the temperature changes at each fumarole. No correlation was found between the background temperature and the fumarole temperatures (i.e. ambient temperature has little influence on the fumaroles).

To determine the spatial variations of the fumaroles, the number of pixels with a pixel-integrated temperature of more than 2°C above the background temperature (or $\Delta T > 2°C$) were counted for each fumarole area (range from 0 to 9 pixels). These values, multiplied by the total area of the pixel (8100 m^2), were used to give an estimate of the overall maximum spatial extent of the fumaroles (range from 0 to ~73 000 m^2). The threshhold value of $\Delta T = 2°C$ is used as it is greater than the error from the Temperature/Emissivity Separation algorithm (±1.5°C) (Gillespie et al., 1999).

For this study, we find that a threshold value of $\Delta T = 2°C$ is sufficient to isolate the thermal anomalies caused by the fumaroles at Aluto. This is much lower than previous studies. Although Pieri & Abrams (2005) state that the Noise Equivalent ΔT of the ASTER instrument (i.e. its sensitivity) is 0.3 - 0.5°C, they also state that practical values used for ΔT are more often 3-5 °C. Jay et al. (2013)

use the pixels with ΔT > 4°C; Vaughan et al. (2014) use values from 1 to 4 standard deviations above background temperature, which corresponds to a ΔT of 2-15°C. When observing eruptive processes, such as lava dome formation and lava flows, which have very high temperatures and thus high amplitude thermal anomalies, it is possible to use higher detection thresholds (Pieri & Abrams, 2005). In this study however, we are studying lower temperature volcanic processes, where the highest recorded temperature of the fumaroles is 95°C (Kebede et al., 1985). As a result, the temperature anomalies observed in the ASTER images have a much smaller amplitude and the lowest possible threshold is required in order to detect the anomalies.

One of the potential causes for changes in the behaviour of the fumaroles is seasonal variation in precipitation. To investigate this hypothesis, data from the Climatic Research Unit (CRU TS v3.22, data from 2004-2014) was used to assess the influence of precipitation on the temperature of the fumaroles. The CRU dataset is a gridded climate dataset interpolated from monthly observations at meteorological stations around the world, covering the land surface with 0.5° latitude/longitude cells (Harris et al. 2014). Studies comparing the data from the CRU model to data from rain gauges in Ethiopia agree that the CRU dataset provides a reliable estimate of precipitation (e.g.: correlation = 0.81-0.95 in central-northern Ethiopia) (Dinku et al., 2008; Tsidu, 2012; Degefu et al. 2016).

3.4. Quantification of the subpixel temperature and spatial changes

The area of the fumaroles is smaller than that of the pixels, meaning that each pixel is a mixture of fumaroles and unheated ground. As a consequence, the pixel-integrated temperature previously discussed, which is the average of the surface kinetic temperature over the total area of the pixel (Gillespie et al., 1999; Harris, 2013), does not directly reflect the actual temperature of the fumaroles. Similarly, the number of pixels above a certain threshold value may not fully reflect the area of ground covered by fumaroles. In order to estimate the actual fumarole temperature and spatial variations, it is necessary to consider the subpixel level.

Assuming an average temperature for the background, T_b, and for the fumaroles, T_f, and assuming linear mixing of the temperatures, the pixel-integrated temperature, T_P, can be calculated by using the following equation:

$$A_P T_P = A_b T_b + A_f T_f \qquad \textit{Equation (1)}$$

where A_P is the total area of the pixel (8100 m^2), A_f is the area covered by the fumaroles and A_b is the remaining of the area of the pixel. By defining ΔT as T_P - T_b, equation (1) can be derived to obtain an estimate of ΔT as a function of T_f and A_f:

$$\Delta T = A_f / A_P * (T_f - T_b) \qquad \textit{Equation (2)}$$

Equation (2) has two unknowns: the area of the fumaroles (A_f) and their temperature (T_f), so assumptions need to be made about one of the parameters so as to extract the other. We start with end-member assumptions – first that T_f remains constant and any variations in ΔT are a result of changes in A_f, and secondly that A_f remains constant and any variations in ΔT are a result of changes in T_f. These scenarios are not taken to represent the real situation as in reality both conditions are likely to vary together. However they give an indication of how each parameter affects the temperature variations.

For the first scenario, values for T_f can be assumed using the temperature measurements collected on the ground in order to estimate the change in A_f (minimum = 65°C, maximum = 95°C). The results show that theoretically, according to the detection threshold used in this study (ΔT = 2°C), a fumarole with a ground temperature of 65°C needs to cover at least 4% of a pixel (324 m^2) in order to be detected in an ASTER image. A hotter fumarole with a ground temperature of 95°C needs to cover 2.4% of a pixel (194 m^2) (***Figure 4a***).

For the second scenario, we assume that fumarole field areas range between 100 m^2 and 350 m^2 (***Figure 4b***). These values correspond to the typical values obtained from Equation 2 for known values of T_f. A fumarole field covering an area of 100 m^2 needs to have a temperature greater than 150°C to be detected in the ASTER images (ΔT > 2°C). A fumarole field covering an area of 350 m^2 only needs to have a temperature greater than 30°C to be detected. These estimates give an indication of the spatial limits of the detection threshold of the ASTER images.

4. Results

4.1. Fumarole identification and classification

We classify the fumarole areas identified on Aluto during the period of this study into three classes. Class 1 fumaroles correspond to the areas where clusters of 3-13 pixels with a ΔT > 2°C appear in more than 2 images; class 2 fumaroles correspond to the areas where 1-2 pixels above background temperature appear in 1-2 images; class 3 fumaroles are the areas which have been located on the ground but cannot be identified in the images. Six fumaroles are defined as class 1 fumaroles, four are identified as class 2 fumaroles and two are identified as class 3 (***Figure 3b***). A set of hot springs were identified on the north-west shoreline of Lake Langano to the south of Aluto. Temperature values from these hot springs were difficult to extract due to their close proximity to the water and to the changing water levels from one image to the next, so these data are not discussed further.

The fumaroles identified in the ASTER images coincide with the hydrothermal areas located on the ground (Kebede et al., 1985; Hutchison et al., 2015, 2016c) (***Figure 3)***. The majority of these areas

are located on or close to faults, in particular the regional AJFZ and the caldera ring fault (***Table 1, Figures 3 and 5)***. The Oitu Artu and Gebiba areas do not appear to be located along any surface structural feature.

The classification used in this study corresponds well to the differences in temperature recorded on the ground. The six class 1 fumaroles correspond to the fumaroles with the highest recorded ground temperature (93-95°C). These are Auto, Hulo, Oitu Artu, Gebiba, Bobesa and the Artu Jawe fumarole region (***Figure 3b***). The Artu Jawe (AJ) area has the largest density of fumaroles on Aluto. Three separate hot areas are identified in the ASTER images and these are named Artu Jawe North, Middle and South (AJN, AJM, AJS) (***Figure 3b***). The four class 2 fumaroles correspond to the medium temperature fumaroles (≈85°C). These are Adonshe, Worbota, Finkilo and Kore (***Figure 3b***). Finally, the fumaroles with the lowest recorded ground temperatures (65-77°C) do not appear anomalous in the ASTER images and correspond to the class 3 fumaroles. These are Humo and the hot springs located on the northern shore of Lake Langano (***Figure 3b***). The fumaroles which provide reliable data are the six class 1 fumarole areas as these have an average $\Delta T \approx 3.5 \pm 1.4$ °C, which exceeds the threshold value of $\Delta T = 2$°C. The class 2 fumaroles only have an average $\Delta T \approx 1.6 \pm 0.5$°C. Only the class 1 fumaroles are used for further analysis.

4.2. Changes observed at the fumaroles

The time series of the temperature changes at each fumarole are shown in ***Figure 6***. A summary of the mean ΔT values for each fumarole is provided in Table 1. The majority of the fumaroles on Aluto appear stable and do not show changes in ΔT over time significantly above error of the measurements (± 1.5°C). Gebiba and Auto show the least change in temperature. The majority of the fumarole areas (Oitu Artu, Hulo and the Artu Jawe areas) show temperature variations marginally outside error (***Figure 6, Table 1***). Any trend displayed by these fumaroles cannot be identified with confidence. Bobesa is the only fumarole where temperature varies significantly above the error range. It shows a range of ΔT values from 2.7 to 9.1°C and has the highest mean temperature above background (ΔT = 6°C). These values are comparable to the ranges measured in other volcanic areas (for example in the central and southern Andes: Jay et al., 2013 and at Yellowstone: Vaughan et al., 2014).

The time series of the changes in spatial extent of each fumarole are shown in ***Figure 7***. All the fumaroles show some changes in spatial extent, including the fumaroles that do not show significant temperature changes such as Gebiba and Auto. Bobesa and AJN show the largest areal changes, reaching up to ~73 000 m^2 in pixel area (9 pixels with $\Delta T > 2$°C). Even the fumaroles with the smallest areas (e.g. Gebiba and Hulo) seem to show considerable spatial variation, doubling in pixel area. It should be noted that the actual spatial changes of the fumaroles on the ground occurs on a

subpixel level and are likely to be much smaller than those measured in pixel area. The spatial variations at all the fumaroles are sporadic and on average most of the fumaroles have a relatively constant extent over time. Bobesa is the most extensive as well as the most spatially variable fumarole over time, followed by the AJN fumarole. These observations agree with the studies on the ground that state that the ground alteration around Bobesa is ~1 000 000 m^2, making it the largest alteration area observed in the study area (Kebede et al., 1985). The Artu Jawe Fault zone that hosts the AJN fumaroles is known to be the area where the greatest density of fumaroles is found and is where the productive geothermal wells (LA-3 and LA-6) are located (Kebede et al., 1985; Hutchison et al., 2015) (***Figure 3a***).

The observed temperature and spatial changes are broadly self-consistent. For example, Oitu Artu has the lowest mean ΔT of all the fumaroles as well as the lowest mean spatial extent and Bobesa has the highest. However, the correlation between the temperature and spatial changes is not equally strong for all the fumaroles; Bobesa and AJN show a strong correlation (R^2 = 0.70 and 0.72, respectively) but others are very poor (Hulo, R^2 = 0.10; Gebiba, R^2 = 0.10) (***Figure A.1***). The strong correlation at Bobesa is significant as it supports that the trend observed both in temperature and spatial changes represent a real phenomenon rather than random fluctuations.

4.3 Causes for the temperature and spatial variations observed at Bobesa

Bobesa is the fumarole area that shows the greatest temporal variability. The changes at the Bobesa fumaroles are not linked to seasonal temperature variations as shown by the correlation plots in Figure 8a and 8d. Moreover, the data coverage was found to be insufficient to observe any correlation between temperature changes and the deformation pattern. Only two images were acquired during the uplift episodes in 2004 and 2008. There has been steady deflation at Aluto since 2009, yet no equally steady trend is observed in the behaviour of the fumaroles. Only the data from Bobesa suggests a slight increase in temperature since the deflation began (***Figure 6***).

The effect of precipitation on the hydrological flow in the subsurface is the most likely cause for the observed changes in fumarole behaviour. This effect is not apparent directly after the precipitation has occurred, as shown by the lack of trends in figures 8c or 8f, but the temperature changes according to the time of year (***Figures 8b, 8e***). We anticipate a time lag between when the rain falls on the ground and percolates through to the shallow hydrothermal system, affecting the behaviour of the fumaroles. This time-lag has been shown to be on the order of 1-4 months in other locations (McCoy and Blanchard, 2008; Saibi et al., 2010).

We tested the correlation of the temperature and spatial changes with precipitation data from 1 to 4 months prior to the acquisition of the images. The strongest correlation was identified with the precipitation data 3 months prior to the acquisition of the images for both the temperature and the spatial changes (***Figure 9***), and a weaker correlation with the data from 2 months (***Figure A.2***). The 2-3 month timescale also corresponds to the time lag between the precipitation and the peaks of induced seismicity, which are thought to reflect the recharge of the geothermal reservoir (Wilks et al., 2017). The correlations for the precipitation data 1 and 4 months prior to the acquisition of the images were not as strong (mean R^2 value between the temperature and spatial trends < 0.30) (***Figure A.2***).

The data is consistent with a bi-linear trend in temperature and area: 1) from 0 to 80 mm/month, a decrease in temperature and spatial extent with increasing amounts of rainwater in the system (temperature decrease: $R^2 = 0.33$; area decrease: $R^2 = 0.53$) and 2) from 80-180 mm/month an increase in temperature and area with increasing amounts of precipitation (temperature increase: $R^2 = 0.78$; area increase: $R^2 = 0.59$). Potential mechanisms for this trend are discussed in section 5.3. The precipitation data used in this study gives monthly precipitation averages so it was not possible to look at the effects of precipitation on a shorter timescale.

4.4 Subpixel variations

In this section, we consider subpixel variations in fumarole temperatures and areas and their influence on pixel-integrated values of temperature. The temperature and spatial changes are strongly connected, as demonstrated by the correlation plots (***Figure A.1***). In light of this, our subpixel calculations are used as end-member scenarios to give an indication of how much the temperature and area of the fumaroles would need to change individually in order to lead to the observed changes in pixel-integrated temperature. They are representative rather than actual estimates for the changes occurring at the fumaroles during the period of the study.

First, we assume that fumarole temperature, T_f, is constant, using the ground temperature data available for each fumarole (***Table 1***), and calculate the subpixel spatial variations necessary to cause the changes in pixel-integrated temperature observed. The variations observed at Bobesa, the fumarole that shows the greatest range in overall temperature variation, correspond to a change in subpixel area of ~600 m^2 (***Table 2***). Hulo, one of the fumaroles that shows the smallest overall change in pixel area, would require a more substantial subpixel areal variation (~255 m^2) in order to accommodate the ΔT range observed. The fumaroles with the smallest ΔT range (1-2°C for Auto and Gebiba) show a change in spatial extent of less than 150 m^2.

Next, we assume that the area of the fumaroles, A_f, is constant and calculate the subpixel temperature variations necessary to cause the changes in pixel-integrated temperature observed. The calculations show that given a fixed area, the fumarole temperatures must vary substantially to cause pixel-integrated temperature variations similar to those detected in this study. For Bobesa, a change in

temperature of 170°C is required; for the fumaroles with the smallest ΔT ranges, a change in temperature between 25°C and 100°C (Gebiba, Auto, Oitu Artu) is calculated (***Table 2***). These model temperature changes are unrealistically large, which confirms that spatial changes must also be occurring.

We hypothesise that fumarole temperature variations such as those calculated at Bobesa would likely correspond to a change in the thermo-physical behaviour of the fumaroles where the increase in temperature would lead to higher energy in the system and perhaps increased convection. This would be reflected at the surface by increased boiling and venting of the fumaroles, and by an increase in the fumarole area with the emergence of new vents and the escape of steam through porous ground (D'Auria et al, 2011; Chiodini et al., 2011). The isolation of the subpixel temperature and areal variations is not realistic, and in reality the two scenarios need to be considered together.

5. Discussion

5.1. Low-amplitude thermal anomaly detection

This study has shown that it is possible to detect fumaroles in ASTER TIR images, with a detection threshold for pixel-integrated temperatures of ΔT ~ 2°C. The comparison of the temperatures from the ASTER images with the ground temperatures of the fumaroles shows that only the fumaroles with a ground temperature >93°C can be detected with confidence (***Figure 3b, Table 1***). Fumaroles with a temperature of 85°C can be detected, but only when the location of the fumarole is known (***Figure 3b, Table 1***). This range of temperatures gives an estimate of the detection threshold and the limits of the ASTER images. The subpixel calculations show that fumaroles with a high temperature (95°C) appear on the images providing they have a large enough extent (~200 m^2) (***Figure 4***). Evidence from the field suggests that this is a conservative estimate however, as the hottest fumaroles on the ground usually cover <50 m^2 in area, suggesting that the ASTER images can actually detect much smaller features than estimated by this study.

Previous studies have shown that relatively large temperature and areal changes at fumaroles are not uncommon, with diurnal temperature variations of up to 50°C (Connor et al., 1993). However, the majority of the fumaroles on Aluto show a stable behaviour, manifesting only small temperature variations (ΔT < 2°C). The majority of our images were taken during the cloud-free dry season, and greater short-term variability might be expected during the rainy season, or with more frequent data. On a subpixel level, we have shown that the small variations detected can actually represent significant changes in the thermo-physical behaviour of the fumaroles. Further field evidence is required to determine the contribution of temperature versus spatial changes to account for the temperature variations observed.

5.2. Structural controls on the behaviour of the fumaroles

The two largest fumarole areas in this study, the Bobesa fumaroles and the Artu Jawe fumarole region, do not display the same variations in thermal behaviour. Structural features are known to exert a strong control on the emission of gas, steam and volcanic products at Aluto (Hutchison et al., 2015, 2016c). Therefore, we attribute the difference between fumaroles to differences between the underlying faults and their fracture network.

The AJFZ is the main upflow zone of the hydrothermal fluids on Aluto (Gianelli and Telkemariam, 1993; Hutchison et al., 2015). It was chosen as the location for the Aluto geothermal power plant due to the high fluid temperatures at depth (Hochstein et al., 2017). A strong presence of H_2S is recorded, although it should be noted that this presence was only detected by smell, not by fully quantitative measurements (***Table 1***) (Kebede et al., 1985). The maximum CO_2 flux measured along the AJFZ is 10 000-40 000 g m^{-2} d^{-1} (Hutchison et al., 2015) and the CO_2-$\delta^{13}C$ analysis of soil CO_2 samples from the areas of maximum degassing indicates that the CO_2 has a clear magmatic origin (CO_2-$\delta^{13}C$ values from -4.2‰ to -4.5‰) (Hutchison et al., 2016a). Chemical analyses indicate that Finkilo, a fumarole located on the AJFZ ~250 m south of the Artu Jawe fumarole region, has higher concentrations of H_2S, CO_2 and CH_4 than Bobesa which suggests a greater input of magmatic gases (Gizaw, 1985). These observations all indicate that the AJ fumarole region is strongly connected to the magmatic component of the hydrothermal fluids (***Figure 10***).

The maximum CO_2 flux recorded at Bobesa is 1850 g m^{-2} d^{-1} (Hutchison et al., 2015). This value is relatively high, indicating a magmatic contribution, but it is much lower than along the AJFZ. We infer from this observation that Bobesa is less well connected to the deep magmatic reservoir. Bobesa is situated on the eastern rim of the caldera, on the side closest to the Eastern Plateau. The eastern caldera ring fault is thus one of the first faults to be encountered by the groundwater flow from the rift flanks (***Figure 10***). The correlation of the temperature and spatial variations at Bobesa with the precipitation (***Figure 9***) suggests that the hydrothermal fluids are more strongly connected to the groundwater component. This could indicate that Bobesa is not simply a magmatic fumarole, but has more of the character of a 'fresh' spring associated with the upwelling along the caldera fault of water from the highlands (Ayenew, 2005). Moreover, the hydrothermal fluids at Bobesa are more heavily mixed with N_2 and O_2 (Gizaw, 1985), which is associated with mixing with air or air-saturated water (i.e. such as meteoric water derived from precipitation). These observations corroborate our hypothesis that the Bobesa fumaroles are more strongly connected to the meteoric than the magmatic fluids.

Furthermore, the differences between the behaviour of the fumaroles at Bobesa and the AJ fumarole region might be associated with the depth of the different faults. A deeper fault would penetrate into the geothermal reservoir and have a more direct access to the source of magmatic fluids, whereas a shallower fault would be more influenced by the shallow groundwater flow. Another

interpretation from our observations is that the AJFZ cuts deeper than the caldera rim fault, which is likely given that the AJFZ belongs to a regional fault structure, the Wonji Fault Belt that pre-dates the caldera collapse (Corti, 2009; Hutchison et al., 2016b) (***Figure 10***).

The other fumaroles identified on Aluto are also located on faults but they are situated further from the upflow zone and do not show such clear temperature and spatial variations. It is worth mentioning the Hulo fumarole, which is the third largest fumarole in the area and shows temperature variations just above the detection threshold of 2°C (mean value for Hulo temperatures: $\Delta T = 2.8$). This fumarole is located on the Western flank of Aluto, on the West Aluto fault. It has a different composition, specifically higher NH_4OH, to the other fumaroles on the volcano because the fluids feeding Hulo have travelled further through sedimentary layers (Hochstein, 1983). We hypothesise that the differences in terms of chemistry and thermal behaviour are related to the fact that Hulo is connected to a different fluid influx source, presumably the groundwater which flows down the western side of Aluto from Lake Ziway to Lake Langano (Darling et al., 1996). This variability is only observed at Hulo and not at Auto (300 m north of Hulo) because Hulo is larger and more active and as such displays slightly clearer temperature variation in the ASTER images. Our observations both at Bobesa and Hulo suggest that there are more pronounced thermal variations at the fumaroles on the flanks, where meteoric and/or lacustrine recharge is important.

5.3. Causes for the variations and implications for the magmatic/hydrothermal systems interaction at Aluto

We propose that the changes observed at the Bobesa fumaroles are more strongly influenced by hydrological factors ("top-down" scenario, Section 1). The seasonal precipitation has a delayed effect on the behaviour of Bobesa, which we link to the influx of fresh water into the subsurface with a time-lag of 2-3 months after the precipitation (***Figure 9***). When the system is 'dry' (low precipitation values: 0-20 mm/month), the fumarole has a high temperature as it vents the hot, deep, magmatic component of the hydrothermal fluids. At precipitation values of 20-80 mm/month, the magmatic component is diluted by cold meteoric water resulting in the overall cooling of the system. Finally, at high precipitation rates (>80 mm/month), enhanced circulation occurs with deep penetration of cold water and convection bringing up hot fluids from depth. This results in an increase in the fumarole temperature and spatial extent at the surface.

A positive correlation exists between pixel area and temperature, i.e. higher fumarole temperatures correspond to larger areas (***Figures 9 and A.1***). This suggests that the Bobesa fumaroles are initially cooled by the influx of meteoric water, resulting in a decrease in temperature and area. When an increasing amount of meteoric water enters the system and enhances circulation, the fumarole temperature and area increase again, returning to a background temperature and extent. These

subtleties in subpixel variations cannot be detected in our data however. The bi-linear trend is only observed at Bobesa and observations from other volcanoes or models would be useful to test this hypothesis. In addition, a detailed geochemical study of the He or C isotope systematics ofhydrothermal fluids and gases at the Bobesa fumaroles would be useful to estimate the proportion of magmatic components and hence their connectivity to the deeper reservoirs. This would provide a clearer understanding of the recharge of the geothermal reservoir and whether the time lag observed in this study is also observed in the chemistry of the fluids.

From the images used in this study, it appears that most of the fumaroles on Aluto have a stable long-term behaviour. However, given the strong coupling seen elsewhere between changes in the hydrothermal systems and a) the deformation related to deep magmatic processes (Campi Flegrei: Chiodini et al., 2011; D'Auria et al., 2011 and Yellowstone: Lowenstern & Hurwitz, 2008) and b) the seasonal precipitation (Richter et al., 2004; Di Liberto, 2011), we might expect similar short-term behaviour at Aluto. The inability of our dataset to detect such changes likely reflects the difference in temporal resolution of the studies, highlighting the sparseness of our data. The limited coverage during the periods of uplift in 2004 and 2008 makes it difficult to isolate variations related to magmatic processes with respect to the background seasonal fluctuations, such as those observed at Bobesa. Further monitoring is necessary, either through ground-based monitoring or more frequent satellite observations, in order to achieve a better level of understanding of the magmatic influence on the hydrothermal system at Aluto. If the hydrothermal and magmatic systems are well connected, it is to be expected that episodes of uplift resulting from the injection of new magmatic fluids into the system would lead to an increase in temperature of the fumaroles, particularly along the AJFZ. Indeed, this study has shown that in order to monitor deep changes at Aluto related to changes in the magmatic system, it is best to target the AJFZ fumaroles because the Bobesa fumaroles represent both a magmatic and a precipitation signal.

6. Wider relevance of the study and further work

Firstly, this study has shown that it is possible to correctly identify fumaroles on active volcanoes using remote sensing, which is hugely relevant to the geothermal industry. Tracking the temporal and spatial variations of the fumaroles provides a cost-effective and risk-free way of assessing the geothermal potential of volcanoes and volcanic areas without having to go into the field. The following questions can all be addressed by a careful study of ASTER TIR images: How do the hydrothermal fluids move within the system? Where do they leak out and how sealed is the system? How do the meteoric fluids and seasonal variations affect the behaviour of the fumaroles? These questions provide valuable information when deciding where to locate boreholes. This method does however have some limitations. The fumaroles in this study are identified confidently because

significant background information about Aluto is available (location of fumaroles, general extent of the altered areas and their relation to structural units) (Kebede et al., 1985; Hutchison et al., 2015, 2016c). It is likely that for a volcano where no such records exist, the identification of fumaroles would be more challenging. Moreover, in the case of this study only 20% of the images available from ASTER were useable. In areas of the world where cloud cover is frequent, this number might be even lower, limiting the global applicability of this technique.

Secondly, the use of remote sensing to gain a better understanding of the background thermal activity at volcanoes will allow volcanologists to detect anomalous changes in fumarole activity, which can then be combined with other datasets to evaluate volcanic unrest. In the case of Aluto, it seems that the shallow hydrothermal system is relatively stable although higher temporal resolution than that available from the archive of ASTER acquisitions is necessary to track the immediate response of the hydrothermal system to magmatic movements.

Finally, this study highlights the necessity for understanding the controlling factors behind the interaction between the hydrothermal and magmatic systems at restless volcanoes. This can be achieved by further modelling work (Jasim et al. 2015; Coco et al., 2016) and fieldwork using thermocouples to ground truth and calibrate the TIR estimates. It also emphasises the potential of thermal measurements to understand patterns of hydrothermal circulation and associated fluxes of magmatic components such as CO_2.

7. Conclusions

This study has shown that it is possible to identify low-temperature thermal anomalies at volcanoes using remote sensing techniques. A pixel-integrated temperature of >2°C above the local background temperature is necessary for these anomalies to be detected. On Aluto, the anomalies identified correspond to the hottest fumaroles located on the ground (93-95°C). Most of these do not show any significant temperature changes over time suggesting that the hydrothermal system is relatively stable and unaffected by the long-term processes causing the deformation. This supports the hypothesis that the deformation at Aluto is caused by deep magmatic processes rather than by the shallow hydrothermal system (Hutchison et al., 2016a). In contrast to the other fumaroles, Bobesa shows important temperature and spatial variations, which likely reflect a time-lag effect between precipitation and recharge of the geothermal reservoir. No correlation is observed between the changes at Bobesa and the deformation pattern, which suggests that the deep magmatic system and the shallow hydrothermal system at Aluto are not strongly connected, although this needs to be confirmed by shorter-timescale, higher resolution studies.

Acknowledgements

J. Biggs, I.M.Watson, W. Hutchison, T.A. Mather and D.M. Pyle are members of the NERC Centre for the Observation and Modelling of Earthquakes, Volcanoes and Tectonics (COMET). This work forms a contribution to the NERC Large Grant RiftVolc (NE/L01372X/1) awarded to J. Biggs. W. Hutchison was funded by NERC studentship NE/J5000045/1. I.M. Watson is part of the NASA-ASTER science team and acknowledges NASA and JAXA for the provision of data.

References

Agostini, A., M. Bonini, G. Corti, F. Sani, and P. Manetti (2011a). Distribution of Quaternary deformation in the central Main Ethiopian Rift, East Africa, *Tectonics*, 30, TC4010, doi:10.1029/2010TC002833

Agostini A., Bonini M., Corti G., Sani F. & Mazzarini F. (2011b). Fault architecture in the Main Ethiopian Rift and comparison with experimental models: Implications for rift evolution and Nubia-Somalia kinematics. *Earth Planet. Sci. Lett.*, 301(3-4), 479-492, doi:10.1016/j.epsl.2010.11.024

Arnórsson S., (1995). Geothermal systems in Iceland: structure and conceptual models – I. High-temperature areas. *Geothermics*, 24, 564-602, doi:10.1016/0375-6505(95)00025-9

Aspinall W., Auker M., Hincks T., Mahony S., Nadim F., Pooley J., Sparks R. S. J. & Syre E. (2011). Volcano hazard and exposure in GFDRR priority countries and risk mitigation measures, *In* Volcano Risk Study 0100806-1-R, Global Facil. For Disaster Reduct. And Recovery, Washington, D. C.

Biggs J., Bastow I. D., Keir D. & Lewi E. (2011). Pulses of deformation reveal frequently recurring shallow magmatic activity beneath the Main Ethiopian Rift, *Geochemistry, Geophysics, Geosystems*, 12(9), 1-11, doi: 10 .1029 /2011GC003662

Biggs J., Robertson E. & Cashman K. (2016). The lateral extent of volcanic interactions during unrest and eruption., Nat. Geosci., 9, 308–311, doi:10.1038/ngeo2658

Carter A. J & Ramsey M. S. (2009). ASTER- and field-based observations at Bezymianny Volcano: Focus on the 11 May 2007 pyroclastic flow deposit. *Remote Sensing the Environment*, 113, 2142-2151, doi: 10.1016/j.rse.2009.05.020

Chiodini G., Avino R., Caliro S. & Minopoli C., (2011).Temperature and pressure gas geoindicators at the Solfatara fumaroles (Campi Flegrei). *Annals of Geophysics*, 54, 2, 175-185, doi: 10.4401/ag-5002

Chorowicz J. (2005). The East African Rift system. *J. African Earth Sciences*, 43, 379-410, doi:10.1016/j.jafrearsci.2005.07.019

Coco A., Gottsmann J., Whitaker F., Rust A., Currenti, G., Jasim A. & Bunney S. (2016). Numerical models for ground deformation and gravity changes during volcanic unrest: simulating the hydrothermal system dynamics of a restless caldera. *Solid Earth*, 7, 557-577, doi: 10.5194/se-7-557-2016

Connor C. B., Clemet B. M., Song X., lane S. B. & West-Thomas J. (1993). Continuous monitoring of high-temperature fumaroles on an active lava dome, Volcan Colima, Mexico: Evidence of mass flow variation in response to atmospheric forcing. J. Geophys. Res., 988(B11), 19713-19722, doi: 10.1029/93JB02169

Corti G. (2009). Continental rift evolution: From rift initiation to incipient break-up in the Main Ethiopian Rift, East Africa. *Earth Science Reviews*, 96, 1-53, doi: 10.1016/j.earscirev.2009.06.005

Darling W., Gizaw B. & Arusei M. (1996). Lake-groundwater relationships and fluid-rock interaction in the East African Rift Valley: isotopic evidence. *Jour. of African Earth Sciences*, 22(4), 423-431, doi: 10.1016/0899-5362(96)00026-7

D'Auria, L., Giudicepietro F., Aquino I., Borriello G., Del Gaudio C., Lo Bascio D., Martini M., Ricciardi G. P., Ricciolino P. & Ricco C. (2011). Repeated fluid transfer episodes as a mechanism for the recent dynamics of Campi Flegrei caldera (1989–2010), *J. Geophys. Res.*, 116, B04313, doi:10.1029/2010JB007837

Dehn J., Dean K. G. & Engle K. (2000). Thermal monitoring of North Pacific volcanoes from space. *Geology*, 28 (8), 755-758, doi: 10.1130/0091-7613(2000)28<755:TMONPV>2.0.CO;2

Dehn J., Dean K. G., Engle K. & Izbekov Pavel (2002). Thermal precursors in satellite images of the 1999 eruption of Shishaldin Volcano. *Bull. Volcanol.*, 64, 525-534, doi: 10.1007/s00445-002-0227-0

Di Liberto I. S. (2011). Long-term variations of fumarole temperatures on Vulcano Island (Italy). *Annals of Geophysics*, 54 (2), 175-185, doi: 10.4401/ag-5183

ELC Electroconsult, 1986. Exploitation of Langano-Aluto geothermal resources feasability study. Tech. Rep., Ministry of Mines and Energy, Milano, Italy, 289 p.

Fournier, R. O. (1999). Hydrothermal processes related to movement of fluid from plastic into brittle rock in the magmatic-epithermal environment. *Economic Geology*, *94*(8), 1193-1211

Fournier T. J., Prtichard M. E. & Riddick S. N. (2010). Duration, magnitude, and frequency of subaerial volcano deformation events: New results from Latin America using InSAR and a global synthesis. *Geochem. geophys, geosys.*, 11, Q01003, doi: 10.1029/2009GC002558

Gebregzabher Z. (1986). Hydrothermal alteration minerals in Aluto Langano geothermal wells, Ethiopia. *Geothermics*, 15(5/6), 735-740, doi: 10.1016/0375-6505(86)90086-6

Gianelli G. & Telkemariam M. (1993). Water-rock interaction processes in the Aluto-Langano geothermal fields (Ethiopia). *Jour. of Volc. and Geotherm. Res.*, 56(4), 429-445, doi; 10.1016/0377-0273(93)90007-E

Gibson I. L. (1974). A review of the geology, petrology and geochemistry of the Volcano Fantale, *Bull. Volcanol.*, 38, 791-802, doi: 10.1007/BF02596908

Gillespie, A. R., Rokugawa, S., Hook, S. J., Matsunaga, T., & Kahle, A. B. (1999). Temperature/emissivity separation algorithm theoretical basis document, version 2.4. *NASA/GSFC, Greenbelt, MD*

Gizaw B. (1985). The chemistry of geothermal fluids in geothermal areas of the Lakes District, Ethiopian Rift Valley. UNU Geothermal Training Programme, National Energy Authority

Gizaw B. (1993). Aluto-Langano geothermal field, Ethiopian rift valley, physical characteristics and the effect of gas on well performance. *Geothermics*, 22(2), 101-116, doi: 10.1016/0375-6505(93)90050-W

Gleeson, M.L., Stock, M.J., Pyle, D.M., Mather, T.A., Hutchison, W., Yirgu, G. and Wade, J., (2017). Constraining magma storage conditions at a restless volcano in the Main Ethiopian Rift using phase

equilibria models. *Jour. of Volc. and Geotherm, Res.* (in press), https://doi.org/10.1016/j.jvolgeores.2017.02.026.

Gottsmann, J., Folch, A., & Rymer, H. (2006). Unrest at Campi Flegrei: A contribution to the magmatic versus hydrothermal debate from inverse and finite element modeling. *J. Geophys. Res.*, 111 (B7), doi: 10.1029/2005JB003745

Harris, I., P. Jones, T. Osborn, and D. Lister (2014). Updated high-resolution grids of monthly climatic observations—The CRU TS3.10 Dataset. , *Int. J Climatol*., 34, 623–642, doi: 10.1002/joc.3711

Hemmings B., Gottsmann J., Whitaker F. And Coco A. (2016). Investigating hydrological contributions to volcano monitoring signals: a time-lapse gravity example. *Geophys.J Int.*, 207, 259-273, doi: 10.1093/gji/ggw266

Hochstein M. P. (1983). Results of temperature measurements in shallow drill holes, Langano geothermal prospect (Lake District Rift, Ethiopia). Geothermal Institute, University of Auckland, N. Z. Report

Hochstein, M.P., Oluma, B. & Hole, H. (2017). Early exploration of the Aluto geothermal field, Ethiopia (History of discovery well LA-3). *Geothermics*, *66*, 73-84, http://dx.doi.org/10.1016/j.geothermics.2016.11.010

Hurwitz, S., K. L. Kipp, S. E. Ingebritsen, and M. E. Reid (2003). Groundwater flow, heat transport, and water table position within volcanic edifices: Implications for volcanic processes in the Cascade Range, J. Geophys. Res., 108(B12), 2557, doi: 10.1029/2003JB002565

Hutchison W., Mather T. A., Pyle D. M., Biggs, J. & Yirgu, G. (2015). Structural controls on fluid pathways in an active rift system: A case study of the Aluto volcanic complex. *Geosphere*, *11*(3), 542-562, doi: 10.1130/GES01119.1

Hutchison, W., J. Biggs, T. A. Mather, D. M. Pyle, E. Lewi, G. Yirgu, S. Caliro, G. Chiodini, L. E. Clor, and T. P. Fischer (2016a), Causes of unrest at silicic calderas in the East African Rift: New constraints from InSAR and soil-gas chemistry at Aluto volcano, Ethiopia, *Geochem. Geophys. Geosyst*., 17, doi:10.1002/2016GC006395

Hutchison W., Pyle D.M., Mather T.A., Yirgu G., Biggs J., Cohen B.E., Barfod D.N. & Lewi E. (2016b) The eruptive history and magmatic evolution of Aluto volcano: new insights into silicic peralkaline volcanism in the Ethiopian rift, *Jour. of Volc. and Geotherm. Res.*, doi: 10.1016/j.jvolgeores.2016.09.010

Hutchison W., Fusillo R., Pyle D.M., Mather T.A., Blundy J., Biggs J., Yirgu G., Cohen B.E., Brooker R., Barfod D.N. & Calvert A.T. (2016c) A pulse of mid-Pleistocene rift volcanism in Ethiopia at the dawn of modern humans, *Nature Communications*, doi: 10.1038/ncomms13192

Ingebritsen S. E. & Sorey M. L. (1988). Vapor-dominated zones within hydrothermal systems: evolution and natural state. *Jour. Geophys. Res.*, 93 (B11), 13635-13655, doi: 10.1029/JB093iB11p13635

Ingebritsen, S. E., S. Geiger, S. Hurwitz, and T. Driesner (2010). Numerical simulation of magmatic hydrothermal systems, *Rev. Geophys*., 48, RG1002, doi:10.1029/2009RG000287

Jasim A., Whitaker F. F., Rust A. C. (2015). Impact of channelized flow on temperature distribution and fluid flow in restless calderas: Insight from Campi Flegrei caldera, Italy, *J. Volcanol. Geotherm. Res*, 303, 157-174, doi: 10.1016/j.jvolgeores.2015.07.029

Jay. J. A., Welch M., Pritchard M. E., Mares P. J., Mnich M. E., Melkonian A. K., Aguilera F., Naranjo J. A., Sunagua M. & Clavero J. (2013). Volcanic hotspots of the central and southern Andes as seen from space by ASTER and MODVOLC between 2000 and 2010. In:
Pyle D. M., Mather T. A. & Biggs T. (eds) *Remote Sensing of Volcanoes and Volcanic Processes: Integrating Obseravtion and Modelling*. Geological Society, London, Special Publications, 380

Kebede. S, Mamo T. & Abebe T. (1985). Explanation to the Geological Map of Aluto-Langano Geothermal Area., Tech. Rep., Ethiopian Institute of Geological Surveys, Addis Ababa, Ethiopia

Kebede S. (2014). Status of geothermal exploration and development in Ethiopia. From: *Proceedings, 5th African Rift Geothermal Conference*, Arusha, Tanzania

Kogan, L., S. Fisseha, R. Bendick, R. Reilinger, S. McClusky, R. King, and T. Solomon (2012), Lithospheric strength and strain localization in continental extension from observations of the East African Rift, J. Geophys. Res., 117, B03402, doi:10.1029/2011JB008516

Laiolo, M., Coppola, D., Barahona, F., Benítez, J.E., Cigolini, C., Escobar, D., Funes, R., Gutierrez, E., Henriquez, B., Hernandez, A. and Montalvo, F., 2017. Evidences of volcanic unrest on high-temperature fumaroles by satellite thermal monitoring: The case of Santa Ana volcano, El Salvador. *Jour. of Volc. and Geoth.Res.,* (in press), https://doi.org/10.1016/j.jvolgeores.2017.04.013.

Lowenstern J. B., & Hurwitz S., (2008). Monitoring a Supervolcano in Repose: Heat and Volatile Flux at the Yellowstone Caldera, *Elements*, 4, 35–40, doi: 10.2113/GSELEMENTS.4.1.35

Lowell R. P., Van Cappellen & Germanovich L. N. (1993). Silica Precipitation in Fractures and the Evolution of Permeability in Hydrothermal Upflow Zones. *Science*, 260, 192-201, doi: 10.1126/science.260.5105.192

Madonia P. & Fiordilino E. (2013). Time variability of low-temperature fumaroles at Stromboli island (Italy) and its application to volcano monitoring. *Bull. Volcanol.*, 75:776, doi: 10.1007/s00445-013-0776-4

McCoy K. J. & Blanchard P. J (2008). Precipitation, ground-water hydrology, and recharge along the eastern slopes of the Sania Mountains, Bernadillo County, New Mexico. *U.S. Geological Survey Scientific Investigation Report 2008-5179*

Parks M.M., Moore J., Papanikolaou X., Biggs J., Mather T.A., Pyle D.M., Raptakis C., Paradissis D., Hooper A., Parsons B. & Nomikou P. (2015). From quiescence to unrest – 20 years of satellite geodetic measurements at Santorini volcano, Greece. *Journal of Geophysical Research*, 120, 1309-1328, doi:10.1002/2014JB011540

Pieri D. & Abrams M., (2004). ASTER watches the world's volcanoes: a new paradigm for volcanological observations from orbit. *J. Volcanol. Geotherm. Res.*, 135, 13-28, doi: 10.1016/j.jvoleores.2003.12.018

Pieri D. & Abrams M. (2005). ASTER observations of thermal anomalies preceding the April 2003 eruption of Chikurachki colcano, Kurile Islands, Russia. *Remote Sensing the Environment*, 99, 84-94, doi: 10.1016/j.rse.2005.06.012

Pyle, D. M., Mather, T. A. & Biggs, J. (2013). Remote sensing of volcanoes and volcanic processes, integrating observations and modelling – introduction. In: *Remote Sensing of Volcanoes and Volcanic Processes: Integrating Observation and Modelling*. Geological Society, London, Special Publications, 380, 1–13. First published online September 25, 2013, http://dx.doi.org/10.1144/SP380.14

Rampey M.L., Oppenheimer C., Pyle D.M. & Yirgu, G. (2010). Caldera-forming eruptions of the Quaternary Kone Volcanic Complex, Ethiopia. *Journal of African Earth Sciences*, 58, 51–66, doi: 10.1016/j.jafrearsci.2010.01.008

Richter G., Wassermann J., Zimmer M. & Ohrnberger M. (2004). Correlation of seismic activity and fumarole temperature at the Mt. Merapi volcano (Indonesia) in 2000. *J. Volc and Geotherm. Res*, 135, 331-342, doi: 10.1016/j.volgeores.2004.03.006

Saemundsson, K. (2010). Infrared and satellite images, aerial photography. Presented at: *Short Course V on Exploration for Geothermal Resource*, Kenya, Oct. 29 – Nov. 19, 2010

Saibi H., Gottsmann J. and Ehara S. (2010). Post-eruptive gravity changes from 1999 to 2004 at Unzen volcano: a window into shallow aquifer and hydrothermal dynamics. *J. Volc and Geotherm. Res.*, 191, 137-147, doi:10.1016/j.jvolgeores.2010.01.007

Saibi H., Aboud E. & Ehara S., (2012). Analysis and interpretation of gravity data from the Aluto-Langano geothermal field of Ethiopia. *Acta Geophysica*, 60(2), 318-336, doi: 10.2478/s11600-011-0061-x

Salomonson V., Abrams M. J., Kahle A., Barnes W., Xiong X. & Yamaguchi Y. (2010). Evolution of NASA's Earth Observing System and Development of the Moderate-Resolution Imaging Spectroradiometer and the Advanced Spaceborne Thermal Emission and Reflection Radiometer Instruments. In: *Land Remote Sensing and Global Environmental Change: NASA's Earth Observing System and the Science of ASTER and MODIS*, Springer New York, 11, 3-34

Saria, E., E. Calais, D. S. Stamps, D. Delvaux, and C. J. H. Hartnady (2014), Present-day kinematics ofthe East African Rift, *J. Geophys. Res. Solid Earth*, 119, 3584–3600, doi:10.1002/2013JB010901

Stamps, D. S., E. Calais, E. Saria, C. Hartnady, J.-M. Nocquet, C. J. Ebinger, and R. M. Fernandes (2008), A kinematic model for the East African Rift, Geophys. Res. Lett., 35, L05304, doi:10.1029/2007GL032781

Teklemariam M, Beyene K., Berhan Y. A. & Gebregziabher Z. (2000). Geothermal development in Ethiopia. In the Proceedings of World Geothermal Congress 2000, Kyushu - Tohoku, Japan, May 28 - June 10, 2000

Vaughan G. R., Heasler H., Jaworowski C., Lowenstern J. B. & Keszthelyi L. (2014). Provisional maps of thermal area in Yellowstone National Park, based on satellite thermal infrared imaging and field observations. U. S. Geological Survey Scientific Investigations Report 2014-5197, 22 p., doi: 10.3133/sir20145137

Vye-Brown C., Sparks R. S. J., Lewi E., Mewa G., Asrat A., Loughlin S. C., Mee K. & Wright T. J. (2016). Ethiopian volcanic hazards: a changing research landscape, In: Wright, T. J., Ayele, A., Ferguson, D. J., Kidane, T. & Vye-Brown, C. (eds). *Magmatic Rifting and Active Volcanism*. Geological Society, London, Special Publications, 420, http://doi.org/10.1144/SP420.18

Wadge G., Biggs J., Lloyd R. & J.-M Kendall (2016). Historical volcanism and the state of stress in the East African Rift System. *Front. Earth Sci.*, 4:86, doi: 10.3389/feart.2016.00086

Wilks M., Kendall, J-M., Nowacki, A., Biggs, J., Wookey, J., Birhanu, Y., Ayele, A. & Bedada, T. (2017). Sesimicity associated with magmatism, faulting and hydrothermal circulation at Aluto Volcano, Main Ethiopian Rift. *J. Volcanol. Geotherm. Res.* (in press), doi: 10.1016/j.jvolgeores.2017.04.003

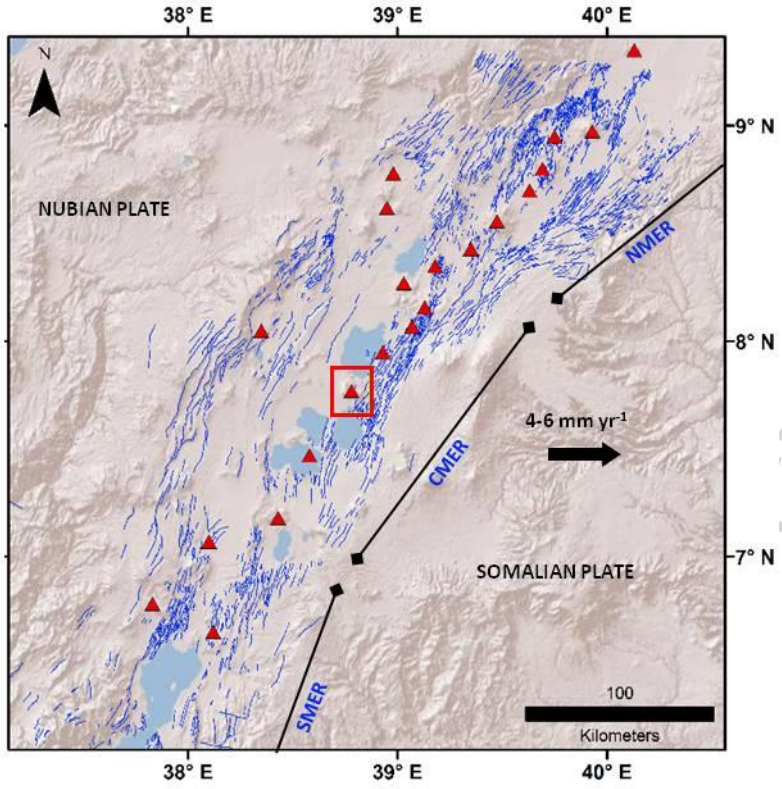

Figure 1 – Map of the tectonic and volcanic features in the Main Ethiopian Rift (MER), divided into the northern MER (NMER), Central MER (CMER) and the southern MER (SMER). The surface faults are shown in blue (mapped by Agostini et al., 2011b, and available at ethiopianrift.igg.cnr.it/utilities_MER.html). The extension rate is 4-6 mm yr^{-1} relative to a fixed Nubian plate (Saria et al., 2014). The red triangles are the Holocene volcanoes listed in Ethiopia (Global Volcanism Program). Aluto is located in the red box in the centre.

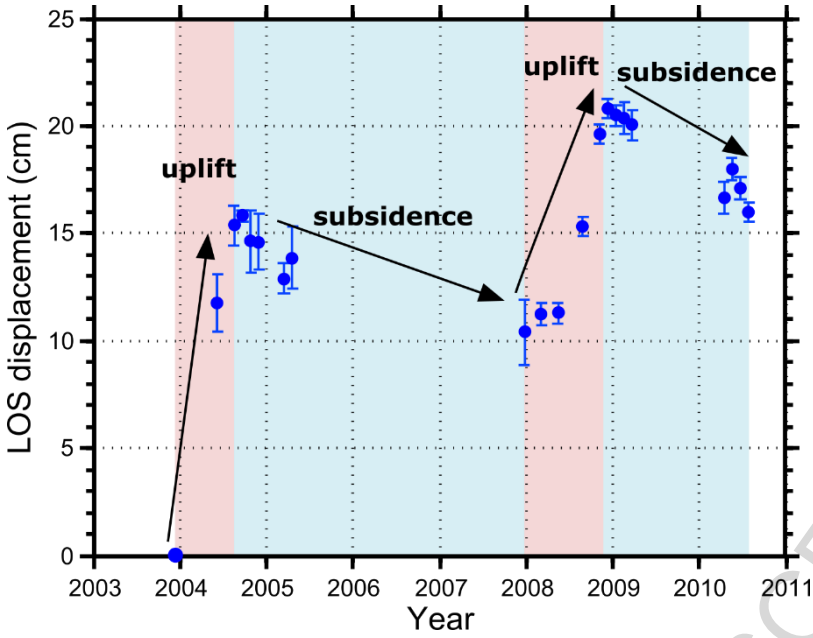

Figure 2 – Displacement time series at Aluto volcano measured by InSAR. Data is from Envisat Image Mode, measured in the satellite line of sight (Biggs et al., 2011; Hutchison et al., 2016a). The two phases of uplift are highlighted by the pink bands.

Figure 3 (next page) – (a) ASTER RGB321 image of Aluto volcano. Fumaroles and hot springs are located by yellow dots and alteration areas are shown by yellow shading (from field studies, details in Kebede et al. (1985); Hutchison et al. (2015)). Geothermal wells are labelled in blue. The faults are mapped in black (Agostini et al., 2011b; Hutchison et al., 2015); **(b)** ASTER image of the surface kinetic temperature on Aluto (AST08). The approximate locations of the fumarole areas used in this study are mapped with black triangles, referring to the coordinates in Table 1. The main fault cutting through the edifice, the Artu Jawe Fault Zone, is labelled AFJZ. Recent obsidian coulees (after Hutchison et al., 2016) are outlined in red dashed lines, several of which have high thermal emissivity and thus appear hot; **(c)** Zoom of the Bobesa and the AJ fumarole regions. AJN is Artu Jawe North, AJM is AJ Middle and AJS is AJ South. The red boxes surrounding each fumarole area are the bounding boxes used to extract the fumarole temperatures over each area. The yellow stars indicate where the photos shown in Figure 5 were taken from.

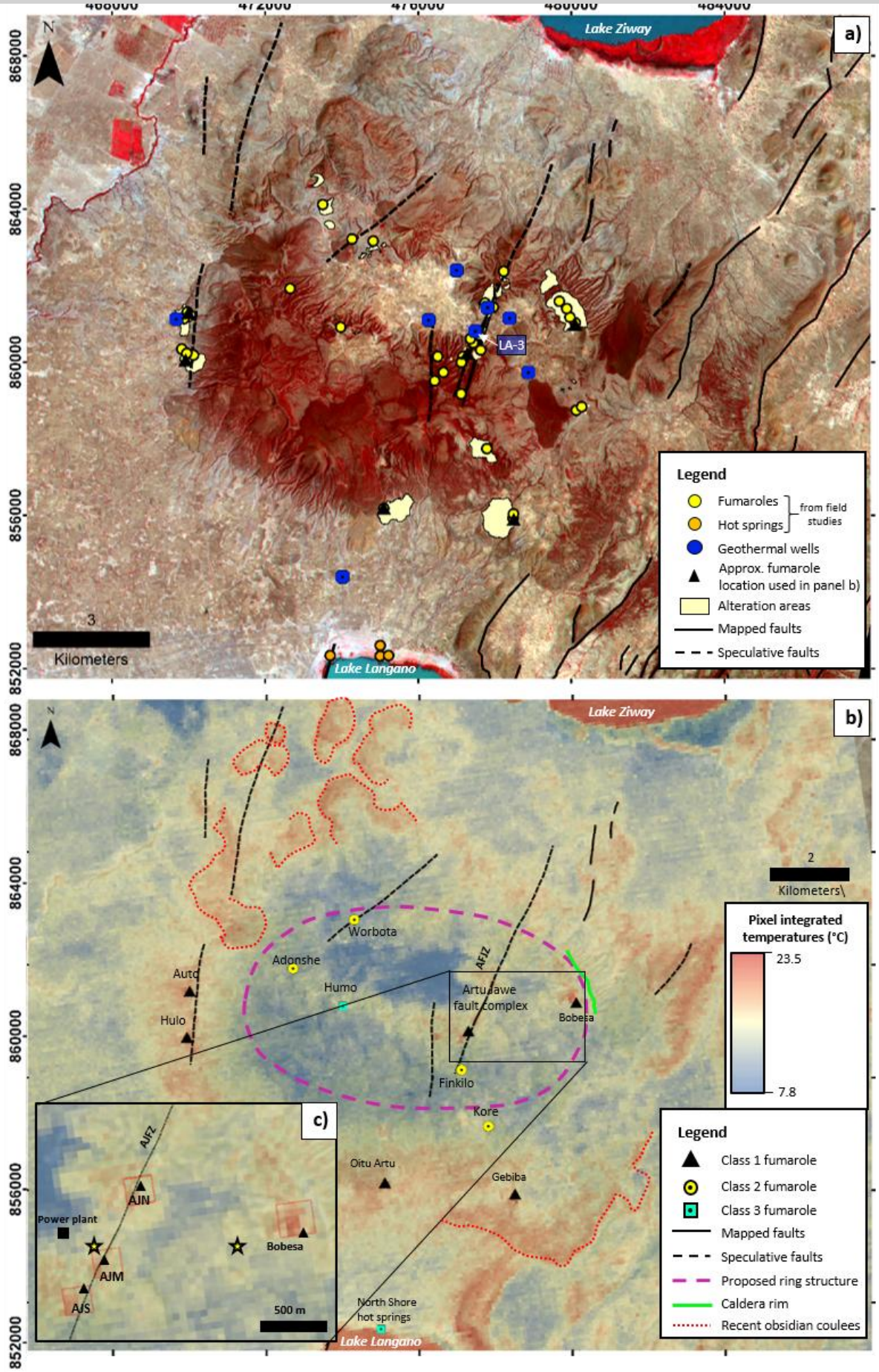

Table 1 – Summary of the relevant information collected about the fumaroles on Aluto, synthesised from Kebede et al., 1985 (*), from Hutchison et al., 2015 ($^{\$}$) and this study. The fumarole areas are shown on the map in Figure 3. The fumarole classification refers to our ability to detect them in the ASTER images. Class 1 fumaroles are the areas where clusters of 3-13 'hot' pixels with a mean temperature above background (ΔT) ≥2°C appear in two or more images; class 2 fumaroles are the areas where 1-2 pixels with a mean ΔT ≤2°C appear only in 1-2 images; class 3 fumaroles are the areas which have been located on the ground but cannot by identified in the images (see Section 4.1).

Fumarole area	**Easting - Northing**	**Ground Temperatures (°C)**	**ΔT in ASTER images (°C)**	**ΔT mean in ASTER images (°C)**	**Spatial variation mean in ASTER images (m^2)**	**Structural association**	**Description of the area**
Class 1 fumaroles							
Auto	470000 - 861300	94*	1.43	2.9 ± 0.43	21355 ± 13685	West Aluto fault	Fumaroles in EW trending gorge Altered ground = 12000 m^2 (*) Significant alteration of pumice to red/orange clays ($^{\$}$)
Hulo	470000 - 860070	95*	2.78	4.14 ± 1.00	30927 ± 8738	West Aluto fault	Altered ground = 35000 m^2, 4 centres of fuming vents (*$^{\$}$)
Oitu Artu	475100 - 856200	94*	2.23	2.35 ± 0.68	13500 ± 16684	Continuation of AJFZ?	Fumaroles set in a deep cut NS gorge Altered ground = 30000 m^2 (*) Located in rhyolite lava, yellow/red clay, strong H_2S smell ($^{\$}$)
Gebiba	478500 - 855900	95$^{\$}$	1.2	3.5 ± 0.32	24300 ± 8460	Hidden NNE-SSW trending fault or lateral outflow from AJFZ?	Altered ground = 540000 m^2, fumaroles = 1000 m^2, in NNE trending deep cut gorge (*) H_2S smell (*$^{\$}$), alteration to red/grey clays ($^{\$}$)
Bobesa	480100 - 861000	93$^{\$}$	6.45	6.02 ± 1.73	43200 ± 34075	Ring fault	Altered ground ~ 1 km^2, hot ground only in central part (*)

							Fumarole vents run in several NW-SE trending ridges, pumices are altered to red/grey clays ($^{\$}$)
Artu Jawe North: AJN	477900 - 861460	95$^{\$}$	2.82	2.89 ± 0.87	30375 ± 25410	AJFZ	Altered ground = 4000 m^2, 13 outlets of steam at junction of two valleys Within 3 km^2 area, 8 groups of fumaroles, to S, N and NE To SW, altered ground = 4000 m^2 area of fuming ground, along NS trending gorge (*) H_2S smell (*$^{\$}$), alteration of surface lithologies to silica and/or carbonates (*$^{\$}$)
Artu Jawe Middle: AJM	477500 - 860500		2.45	2.68 ± 0.59	17550 ± 11881		
Artu Jawe South: AJS	477100 - 860040		1.93	3.45 ± 0.57	29700 ± 11627		
Class 2 fumaroles							
Adonshe	472700 - 861900	85*	0.93	1.52 ± 0.23	--	Continuation of NE-SW fault?	Altered pumiceous ground with fumaroles ($^{\$}$)
Worbota	474300 - 863200	85$^{\$}$	1.86	1.91 ± 0.63	--	NE-SW fault or ring fault?	Steaming ground in small crater and patches of altered ground ($^{\$}$))
Finkilo	477100 - 859200	85*	= 2.03	1.81 ± 0.51	--	AJFZ	Groups of fumarole emanating from rhyolitic lava in NS gorge, H_2S smell, alteration of surface rocks ($^{\$}$)
Kore	477800 - 857700	95*	1.37	1.27 ± 0.43	--	Hidden NNE-SSW trending fault or lateral	Fumaroles aligned in NS gorge, in rhyolite lava ($^{\$}$)

						outflow from AJFZ?	
Class 3 fumaroles							
Humo	474000 - 860900	77*	--	--	--	Unknown	Low temperature fumarole outlets along gorge ($)
North Bay	475000 - 852300	65*	--	--	--	Outflow along water table	Several springs located on northern shore of Lake Langano ($)

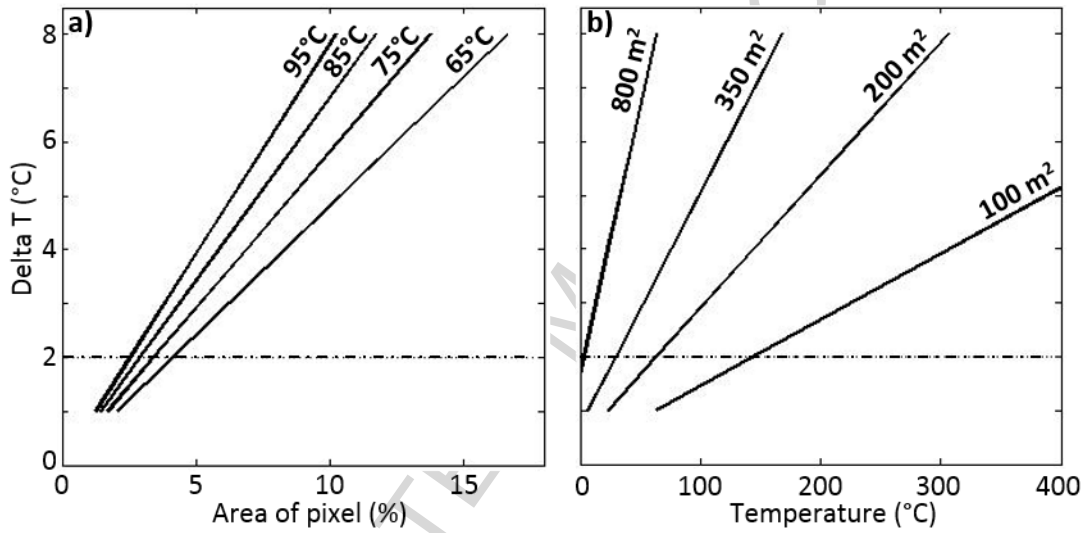

Figure 4 – Sensitivity analysis of ASTER to temperature anomalies based on Equation 2: **a)** temperature anomaly detected (Delta T) as a function of the change in pixel area covered by the fumarole given a fixed fumarole temperature; **b)** temperature anomaly detected as a function of the change in temperature of the fumarole given a fixed fumarole area. The detection threshold used in this study (ΔT = 2°C) is indicated by the dashed line.

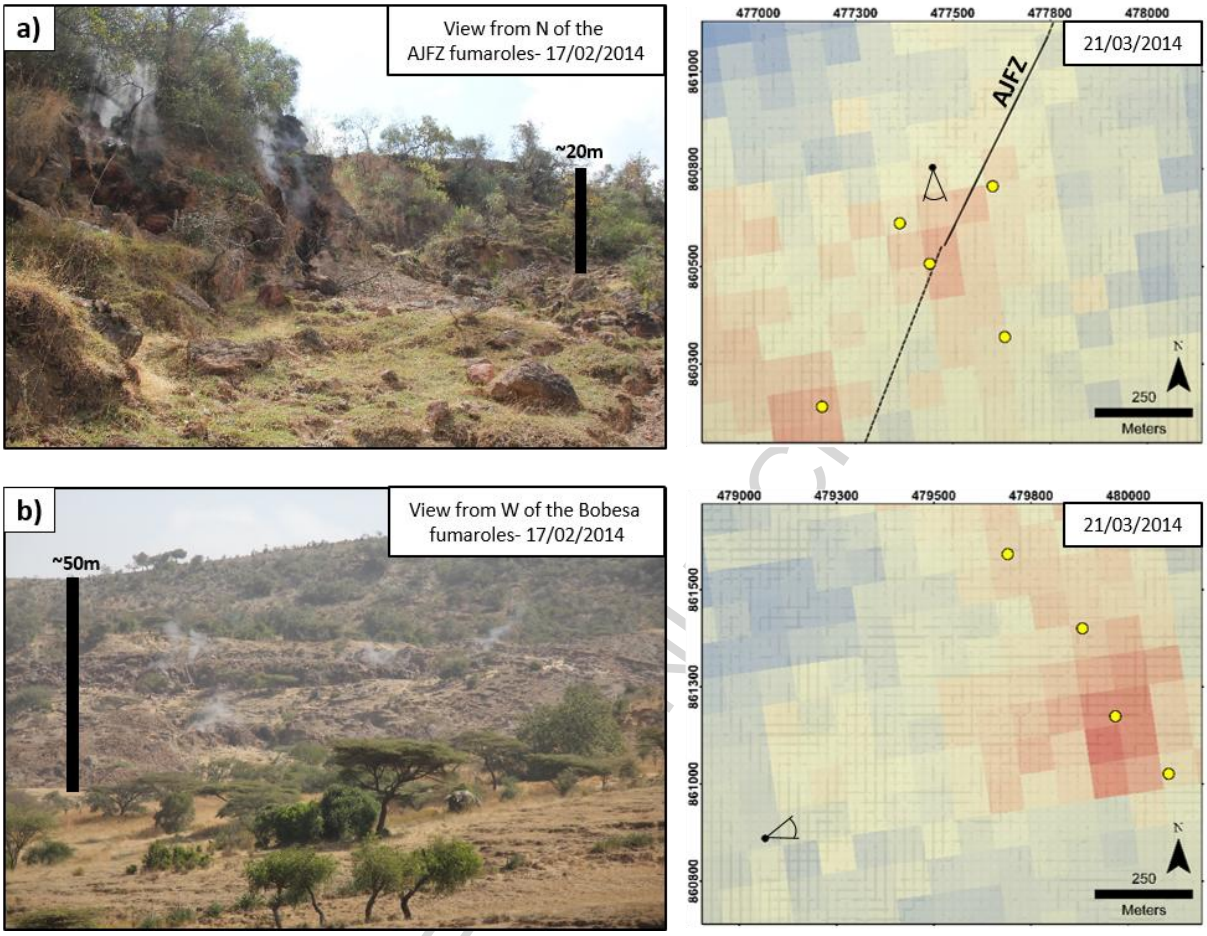

Figure 5 – Comparison of ground and satellite views of selected fumarole areas: **(a)** steam vents along the Artu Jawe Fault Zone (AJFZ). Photo looking south along the fault scarp; **(b)** Bobesa fumaroles. Photo looking east towards the remnants of the caldera rim. Individual fumaroles are vents mapped by Kebede et al. (1985) and are shown by the yellow dots. See Figure 3c for the location of the photos.

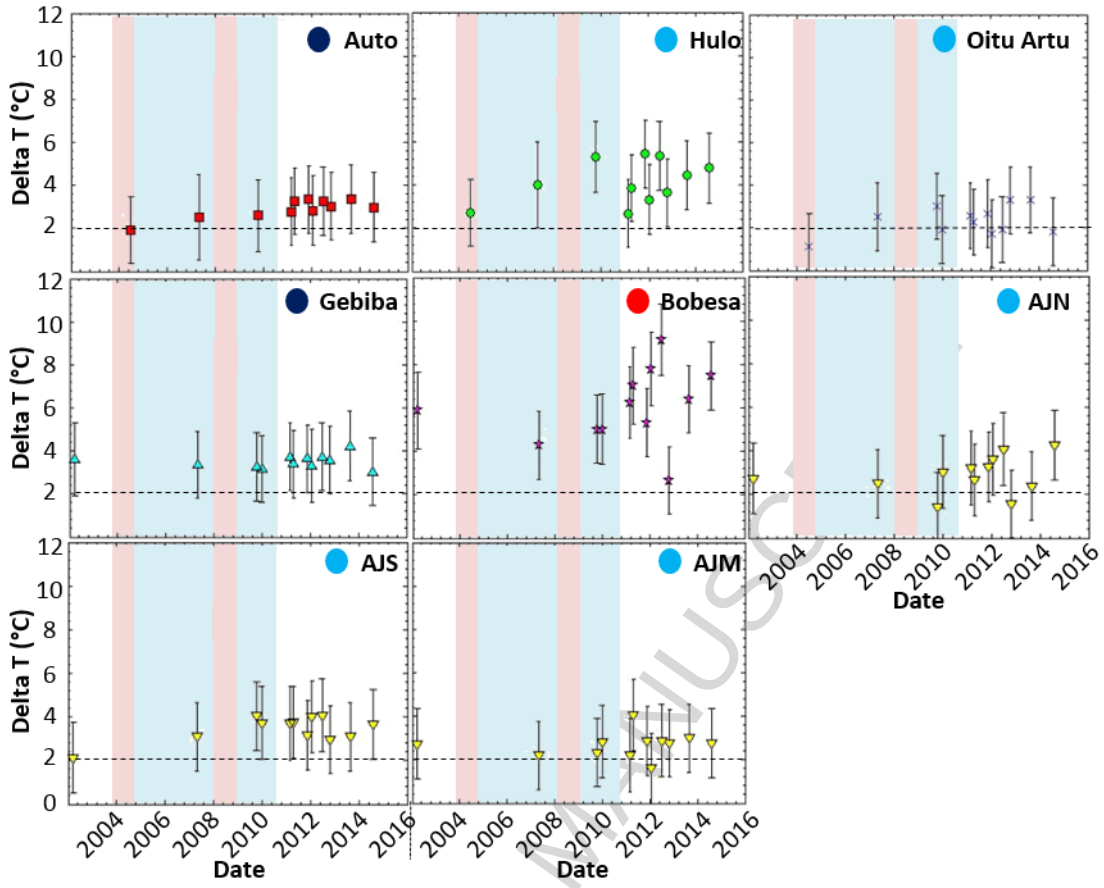

Figure 6 – Temperature change of the hottest pixel from each fumarole over the period of the study. The dashed line represents the 2°C detection threshold used in this study. The error on the temperature values is ± 1.5°C. Fumaroles at which the temperature range is less than the formal error (1.5°C) are considered to have constant temperature, and are marked with a dark blue circle. Fumaroles at which the temperature range is between 1 and 2 times the formal error (1.5-3°C) are marked with a pale blue circle, and those greater than 2 times the formal error (>3°C) are indicated with a red circle. The two phases of uplift are highlighted by the pink bands and the two phases of subsidence by blue bands (Hutchison et al., 2016a; see Figure 2).

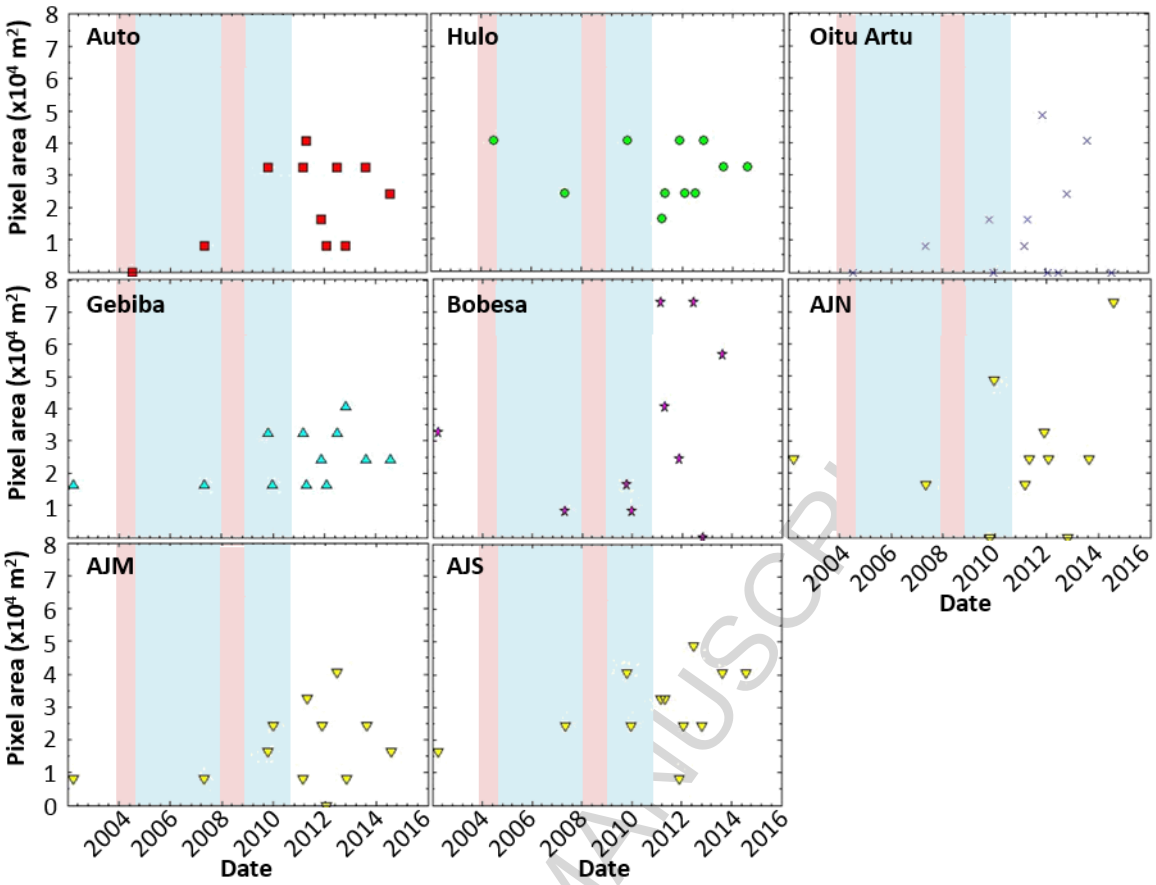

Figure 7 – Spatial change in the extent of the fumaroles over the period of the study, in terms of pixel area (each pixel is 8100 m^2). A pixel area of zero indicates the fumarole did not display any pixels that exceeded the detection threshold of 2°C. The maximum extent detected is 9 pixels with $\Delta T > 2°C$ (≈73,000 m^2). The two phases of uplift are highlighted by the pink bands and the two phases of subsidence by blue bands (Hutchison et al., 2016a; see Figure 2).

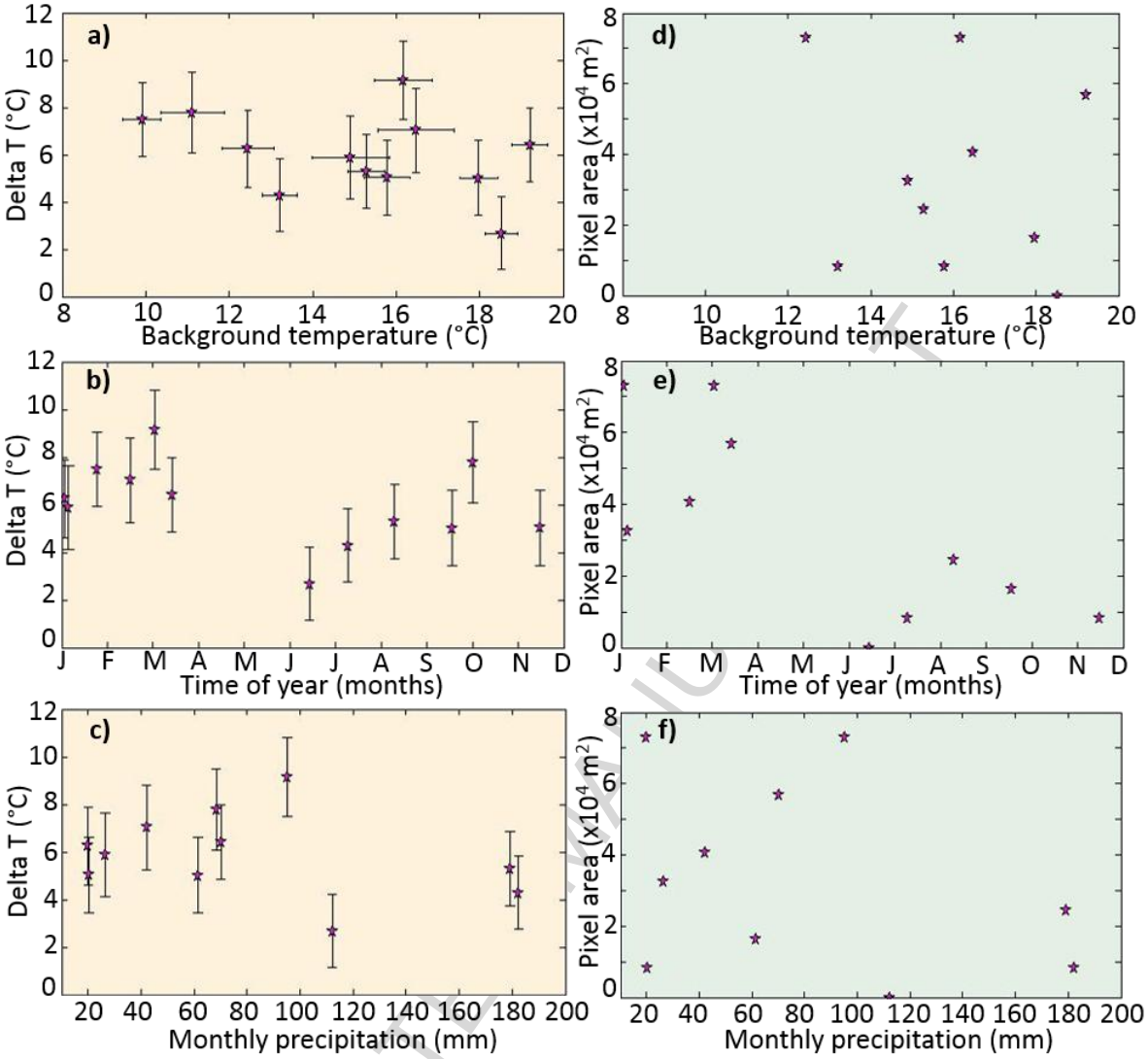

Figure 8 – Assessing the possible causes for the changes observed at Bobesa. Temperature changes: **(a)** as a function of background temperature; **(b)** as a function of seasonality; **(c)** monthly precipitation. Spatial changes: **(d)** as a function of background temperature; **(e)** as a function of seasonality; **(f)** monthly precipitation.

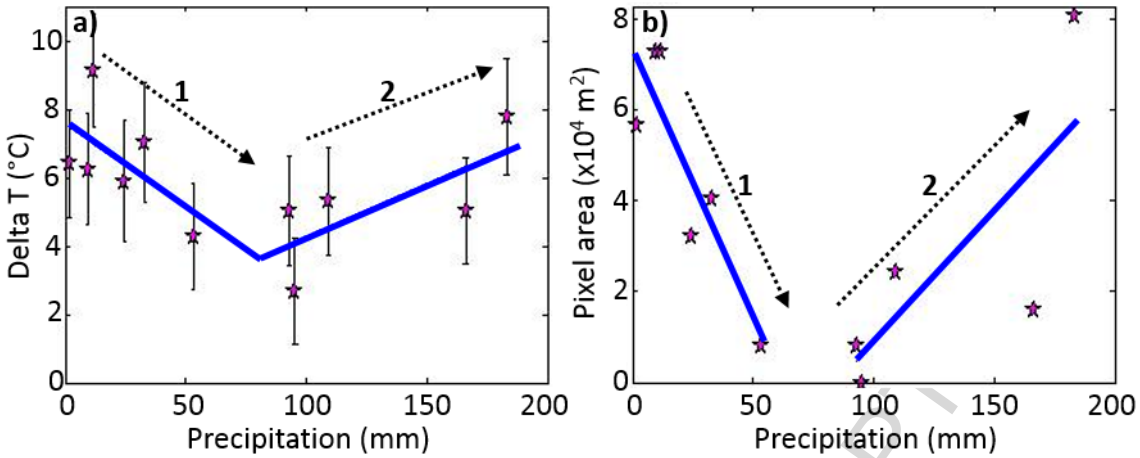

Figure 9 – **a)** correlation of the temperature variations at Bobesa with the precipitation 3 months prior to the acquisition of the image; **b)** correlation of the spatial variations (in terms of number of pixels) at Bobesa with the precipitation 3 months prior to the acquisition of the image. The blue lines represent the trends calculated for precipitation <80 mm/month and >80mm/month. The dashed arrows indicate the processes causing the bi-linear trend in temperature and area: 1) cooling from diluting, cold meteoric water and 2) heating from increased convection and upwelling of hot fluids.

Table 2 – Summary of the subpixel spatial and temperature variations necessary to cause the change in pixel-integrated temperature observed in the ASTER images (ΔT range) over the period of the study at each fumarole.

	ΔT range in ASTER images	**Spatial variations (assuming constant T_f)**		**Temperature variations (assuming constant A_f)**
Fumarole areas in Figure 3b	°C	% pixel	Pixel area (m^2)	°C
Auto	1.9 – 3.4	2.4 – 4	190 – 320	60 – 110
Hulo	2.7 – 5.4	3.5 – 6.6	280 – 535	65 – 150
Oitu Artu	1 – 3.3	1.5 – 4.2	120 – 340	30 – 130
Gebiba	3 – 4.2	3.8 – 4.4	310 – 360	75 – 100
Bobesa	2.7 – 9	3.4 – 11	275 – 890	60 – 230
AJN	1.4 – 4.25	1.8 – 5.2	150 – 420	55 – 210
AJM	1.6 – 4	2.5 – 5	200 – 405	45 – 95
AJS	2.1 – 4.1	2 – 5	160 – 405	70 – 180

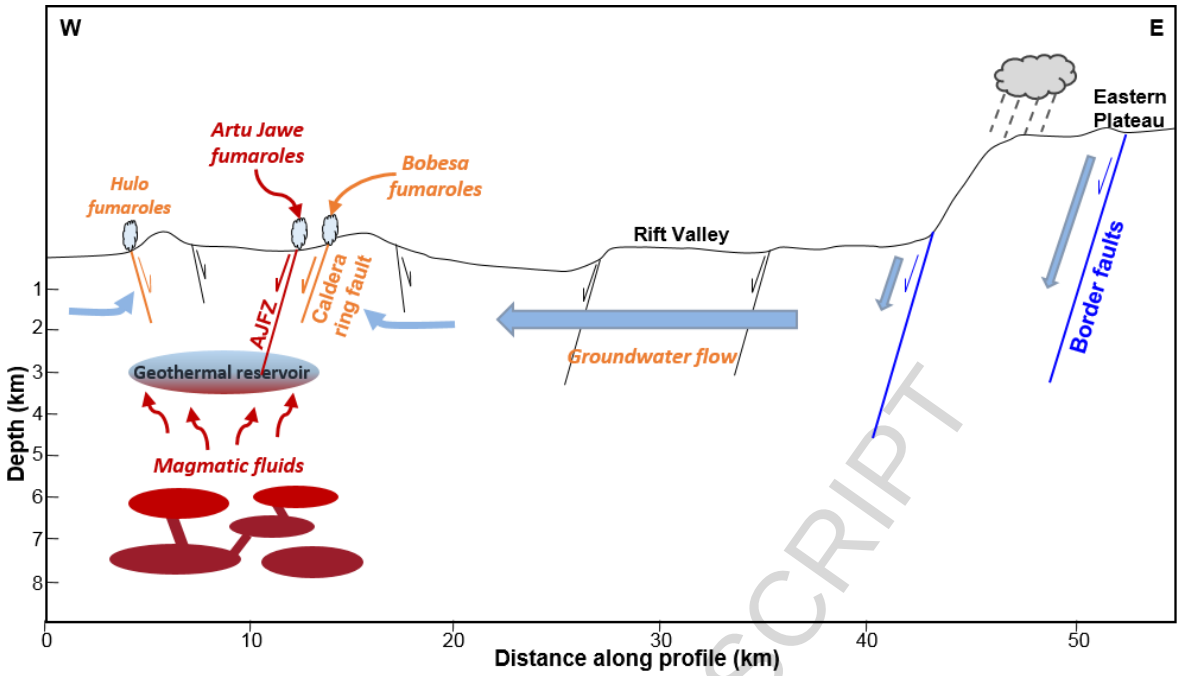

Figure 10 – Schematic cross section of Aluto, showing the hypothesised structural controls on the fumaroles at Aluto. The orange captions highlight the faults and fumaroles influenced by the shallow hydrological processes and the red captions the faults and fumaroles influenced by the deeper magmatic processes.

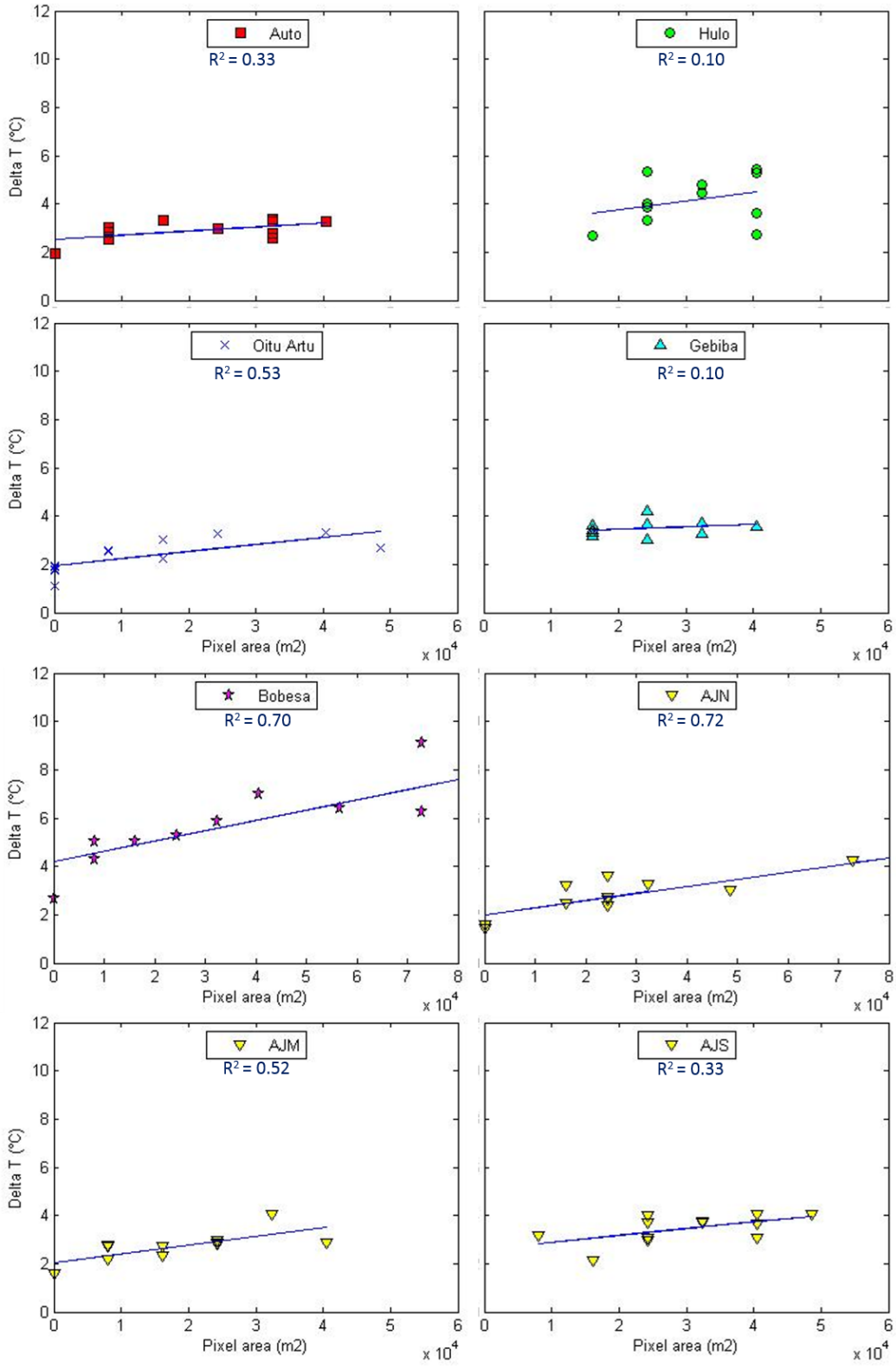

Figure A.1 – Correlation between the temperature changes (ΔT) and the pixel area variations. The coefficient of determination, R_2, is shown for each fumarole.

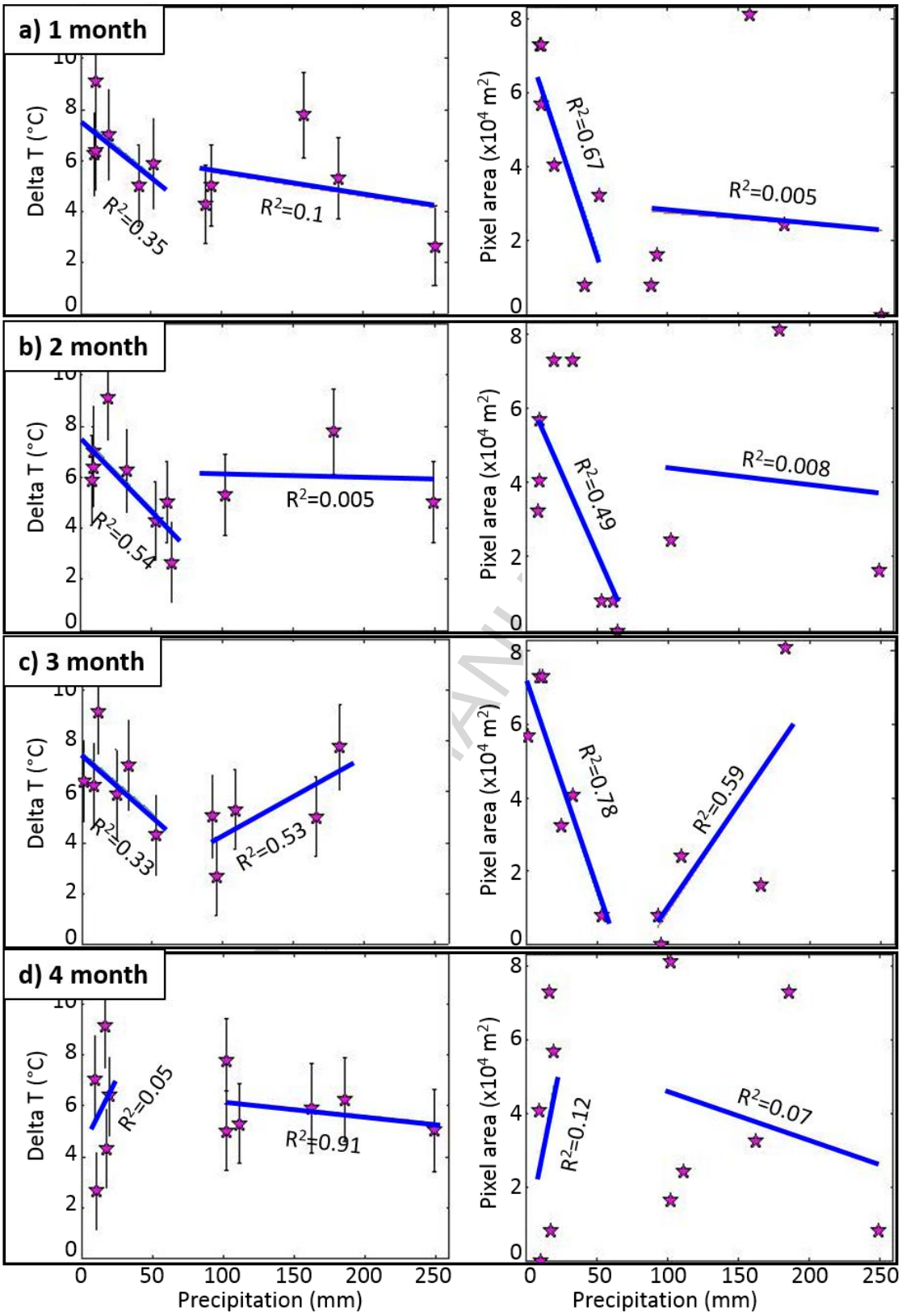

Figure A.2 – Correlation between the precipitation and temperature and spatial variations. **a)** precipitation data 1 month prior to acquisition of image; **b)** 2 months; **c)** 3 months; **d)** 4 month.

Highlights

- Identification of fumaroles on Aluto volcano, MER, using ASTER satellite images.
- Quantification of temperature and spatial variations of the fumaroles and their relation to the hydrothermal and magmatic systems.
- Variations at the Bobesa fumaroles on western caldera rim connected to influx of water from precipitation into the shallow hydrothermal system.
- Artu Jawe Fault Zone fumaroles strongly connected to the magmatic system.